A new population of Terrestrial Gamma-ray Flashes

Master Thesis in Space Physics

by

Nini Lykke Susanne Aandahl Berge

01.06.2017

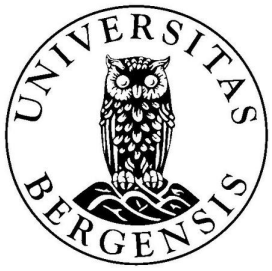

Department of Physics and Technology
University of Bergen
Norway

Abstract

Terrestrial Gamma-ray Flashes (TGFs) consist of large numbers of high-energy photons produced in thunderstorms in connection with the lightning flash, and are the most energetic photon phenomenon naturally occurring on Earth. The satellite RHESSI, originally designed for observing solar flares, is also able to register gamma-rays from Earth.

Algorithms for finding TGFs in the RHESSI data have been purposefully conservative, but *Østgaard et al.* [2015] presented a method to identify TGFs that were not part of previous RHESSI TGF catalogs. By superposing RHESSI data intervals for each lightning detection by the World Wide Lightning Location Network (WWLLN) within RHESSI's field-of-view, they showed that there exists a group of weak signal TGFs.

Expanding on this work we here provide a statistical analysis comparing the signal strength to both background levels and to a Poisson distribution. We seek to optimize the range of the search parameters in order to minimize the chance of including background events. The geographical distribution of the TGFs will also be investigated.

As many of the TGFs we work with have a weak signal, they can be difficult to distinguish from the background level. Because of this the factors that cause variation of the incoming background radiation levels are of interest to us, and we have identify several such factors.

Acknowledgments

First and foremost I want to extend my thanks to my supervisors Prof. Nikolai Østgaard and Kjetil Albrechtsen for providing guidance and support and office doors open for questions at any time.

I would also like to thank the institutions contributing to the World Wide Lightning Location Network and the Reuven Ramaty High Energy Solar Spectroscopic Imager for providing the data used in this thesis.

I thank my fellow master students Anders, Astrid, Bjørn, Chris, Joakim, Kristian, and Roger for the camaraderie and coordinated coffee breaks.

Finally I would like to thank my friends and family for their support and understanding.

Nini Berge

01/06/2017

List of abbreviations

ADELE	*Airborne Detector for Energetic Lightning Emission* (airborne instrument)
AGILE	*Astrorivelatore Gamma a Immagini Leggaro* (satellite)
BATSE	*Burst And Transient Source Experiment* (spaceborne instrument)
CG	*Cloud-to-Ground* (lightning)
CGRO	*Compton Gamma-Ray Observatory* (satellite)
CNES	*Centre National d'Études Spatiales*
ECI	*Earth Centered Inertial* (coordinates)
EIWG	*Earth-Ionosphere Wave Guide*
ESA	*European Space Agency*
FEGS	*Fly's Eye GLM Simulator* (airborne instrument)
FOV	*Field-Of-View*
GLM	*Geostationary Lightning Mapper*
IC	*Intra-Cloud* (lightning)
LIS	*Lightning Imaging Sensor* (spaceborne instrument)
MF	*Middle Frequency* (0.3–3 MHz)
NASA	*National Aeronautics and Space Administration*
RHESSI	*Reuven Ramaty High Energy Solar Spectroscopic Imager* (satellite)

RREA	*Relativistic Runaway Electron Avalanche*
SAA	*South Atlantic Anomaly*
TGF	*Terrestrial Gamma-ray Flash*
TLE	*Transient Luminous Event*
TOA	*Time Of Arrival*
TOGA	*Time Of Group Arrival*
TRMM	*Tropical Rainfall Measuring Mission* (satellite)
VLF	*Very Low Frequency* (3–30 kHz)
WWLLN	*World Wide Lightning Location Network*

Contents

Chapter 1

Introduction

Terrestrial Gamma-ray Flashes (TGFs) are bursts of high energy photons originating in thunderstorms. The photons are in the MeV energy range, and are routinely observed from space. The first observation of TGFs happened in 1991, when the Compton Gamma-ray Observatory (CGRO), looking for gamma-ray bursts of cosmic origin, detected short duration gamma-ray bursts from Earth. The discovery was published by *Fishman et al.* [1994], who were also the first to correlate the bursts with lightning activity.

The CGRO only detected 78 TGFs during its nine year campaign, and while it was known that the CGRO probably only detected very strong events due to their short duration compared to the detector's trigger window, TGFs were viewed as a rare phenomenon.

In 2002 the Reuven Ramaty High Energy Solar Spectroscopic Imager (RHESSI) was launched by NASA, and even though its main objective was to study solar flares, it also detected TGFs at a far higher rate than the CGRO ever did. While the CGRO detected less than one TGF per month on average, *Grefenstette et al.* [2009] identified ∼2.4 TGFs per day during RHESSI's first years of operation. In addition to RHESSI, the satellites AGILE and Fermi were launched in 2007 and 2008, respectively, and are both detecting TGFs at a far higher rate than the CGRO [*Marisaldi et al.*, 2015], [*Briggs et al.*, 2013].

Østgaard et al. [2012] presented a true fluence distribution of RHESSI and Fermi by correcting the measured fluence distributions for their different

orbits, detection rates, and relative sensitivities. The corrected distribution suggested that more TGFs might be produced than what was currently being detected, with the possibility that all lightning could produce TGFs.

With the possible existence of undetected TGFs, *Østgaard et al.* [2015] presented a new method for finding weak signal TGFs. They used lightning registrations done on Earth by the World Wide Lightning Location Network (WWLLN), and searched RHESSI data at the exact time gamma-rays corresponding to each lightning would reach the satellite. By superposing RHESSI data at the time of lightning for all flashes within RHESSI's field-of-view in 2006 and 2012, they successfully identified a population of previously undetected TGFs.

This thesis will be based on this same method, expanding the dataset to the whole period 2002–2015. We will provide a statistical analysis of the parameters that need to be chosen when identifying candidate TGFs, namely their duration, number of counts and the efficient size of RHESSI's field-of-view. We do this with the goal of defining an optimal combination of the parameters in order to get the best statistical significance.

Since the TGFs we study mostly have weak signals, part of the challenge is distinguishing them from the background radiation RHESSI constantly receives. Because of this we will investigate the variation of this background radiation, and try to identify some of the causes why it varies rather than keeping a constant level. We will also study the geographical distribution of the TGFs, focusing on their distribution over ocean and land.

The thesis will open with a summary of the theory behind lightning and TGFs in Chapter 2, followed by previous observations of TGFs in Chapter 3. Our sources of data are described in Chapter 4, and the methodology we use is outlined in Chapter 5. Chapter 6 will present and discuss the results, which are summarized in Chapter 7.

Chapter 2

Theory

In this chapter the theoretical background of this thesis will be presented. The chapter consists of a short introduction to the electrification of thunderclouds and the lightning process. It will then move on to the proposed production mechanisms behind terrestrial gamma-ray flashes.

The thundercloud or lightning itself is not the main topic of this thesis, but we will start with a short overview of some relevant processes in order to have the background needed for further topics. Sections 2.1 and 2.2 are largely based on *Lightning - Physics and effects* by *Rakov and Uman* [2003] and *The Lightning Flash* by *Cooray* [2003].

2.1 Thunderclouds

Lightning primarily occurs in large, anvil-shaped clouds of the type *cumulonimbus*. These form from smaller cumulus fair-weather clouds when warm, moist air rises. If the temperature decreases quickly with height, such rising packets of warm air can stay warmer than the environment, which allows them to keep rising, developing a larger cumulonimbus. As the moist air rises into parts of the atmosphere where the temperature falls below the freezing point, the water particles will start freezing. Some, mainly small, particles will remain liquid in a supercooled state, until the temperature falls to about -40°C [*Rakov and Uman*, 2003].

2.1.1 Cloud electrification

Any explanation of cloud electrification must account for both the charging of individual cloud particles (known as hydrometeors), and the separation of these charges into large-scale charge centers in the cloud. Two of the main mechanisms for cloud electrification that have been proposed are the *convection* and the *graupel-ice* mechanisms.

The convection mechanism suggests that the charges in the electrified thundercloud arise from external sources, namely a positive fair-weather space charge (the charge or the air near the Earth's surface in fair-weather conditions) carried by updrafts into the cloud, and negative charge caused by cosmic rays which is then attracted to the now positively charged cloud. When the rising warm air in the cloud cools off it starts sinking, and through this convective circulation the negative charge is carried down towards the cloud base. This negative charge might also produce a positive corona under the cloud, which then provides positive feedback to the system.

The graupel-ice mechanism suggests that the charge in thunderclouds arises from collisions between graupel that falls downwards and cloud particles of ice and water that hang extended or rise upwards in the cloud. When graupel collides with ice crystals in the presence of supercooled water droplets, laboratory experiments have shown that the graupel acquires a positive charge in temperatures above a certain temperature, T_R, and a negative charge at temperatures below T_R. This temperature dependence would explain the large-scale charge separation in thunderclouds, as the temperature of the atmosphere falls off with height, but the physics behind it are not well understood [*Rakov and Uman*, 2003].

2.1.2 Charge distribution in clouds

Whichever mechanism is actually responsible for the electrification of thunderclouds, the result can be measured. The distribution of electric charges in a cloud can be complicated and variable, but the basic layout is often simplified to a tripole model, where a large positive charge lies above a large

negative charge, with an additional, smaller positive charge towards the bottom of the cloud above a conductive ground. See Figure 2.1.

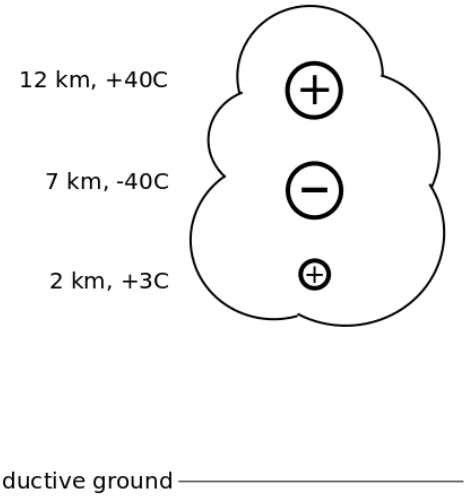

Fig. 2.1: The simple tripole model of the charge distribution in thunderclouds. The three charge centers have their typical heights and charges indicated. Adapted from *Rakov and Uman* [2003].

This model ignores positive space-charge by the ground and a negative screening charge at the top of the cloud, as well as smaller-scale variations and charge regions within the cloud, and the movement due to convective forces. But as lightning mostly happens between one of the main charge centers and the ground or within the cloud between the two main charge centers, this model provides a useful general picture.

The separation of the two main charges can be explained by the convective circulation of the cloud for the convective mechanism of cloud electrification, or by the temperature dependence of the sign of the charge in the graupel-ice mechanism.

2.2 The lightning discharge

Lightning happens when the charges building up in the thundercloud set up an electric field of sufficient magnitude to cause an electrical breakdown of the air. This means that the normally insulating air becomes partially electrically conductive, allowing currents to flow through it. The field strength necessary for break-down to occur in air is about 30 kV/cm [*Cooray*, 2003]. The propagation of the lightning discharge and electrical breakdown will be further discussed in the following section.

2.2.1 Streamer and leader processes

The lightning discharge is a spark of several kilometers' length. For this to occur, a channel of ionized, conductive air is needed. Creating such a channel is not an instantaneous process. The propagation of the ionization of air that allows such a spark to occur is led by filamentary discharges called *streamers*. There are positive and negative streamers, the former traveling with the direction of the electric field, and the latter against it. The processes involved in the creation and propagation of the two types are slightly different.

Positive streamers are created when a free electron in an electric field between a positive (anode) and negative (cathode) charge center creates an electron avalanche. If the electric field around the electron is strong enough, the electron, traveling along the electric field, can "knock off" another electron, which can in turn knock off others. The electrons will travel towards the positive charge region, leaving a positive area of ionized air molecules behind it as electrons are removed. As the avalanche reaches the anode, the electrons will be absorbed. The positive space charge is now by the anode, in practice decreasing the distance between the anode and cathode by extending the positively charged area. Due to recombination of electrons and ions, highly energetic photons are created around the avalanche head. These photons will cause secondary avalanches, and if the positive charge is strong enough, the electrons in these avalanches will be attracted to it. The secondary electron avalanches will again cause a positive space charge behind them as they reach the positive charge area from the first avalanche, this time even closer to the cathode. This process repeats until a streamer, being

a channel of weakly conductive ion-electron plasma, spans the gap between the anode and cathode [*Cooray*, 2003].

Negative streamers, just as positive, start with an initial electron avalanche. Negative streamers, however, propagate from the cathode to the anode rather than the other way around. This happens if the positive space charge behind the initial avalanche is close enough to be attracted towards the cathode. The field enhancement that happens in the region as the positive charge is attracted to the cathode causes the cathode to release electrons. The electrons and the ions of the positive space charge neutralize and form a conductive channel between the avalanche head and the cathode. This process continues as the avalanche progresses in direction of the anode.

The leader

In order for the streamer process to lead to a lightning discharge, they have to change into a *leader*. Each individual streamer channel is only weakly conductive, and the currents involved are not strong enough to heat the air sufficiently for conductivity to increase. But it can happen that several streamers form around a common "stem". This stem will then experience the combined current of all the streamers formed around it, and the air temperature will rise. The gas expansion from the heating allows greater ionization and electron production, and a hot, conductive channel is formed. This channel is the leader, and it is larger, hotter and more conductive than the streamers. Most of the voltage is transferred to the tip of the leader due to the high conductivity, and a high field region is formed there. From this region new streamers can form, eventually allowing the leader to move further in a stepped manner. For the leader to propagate, a field of about 100 kV/m is required [*Cooray*, 2003].

When a leader comes close enough to the conductive ground or to the opposite charge center in the cloud, discharges called *connecting leaders* of the opposite polarity will form due to the high field the leader tip brings. The connecting leader will propagate towards the leader, and where they meet lightning will occur as a large current is transferred through the leader channel, discharging the now connected charge regions.

2.2.2 Types of lightning

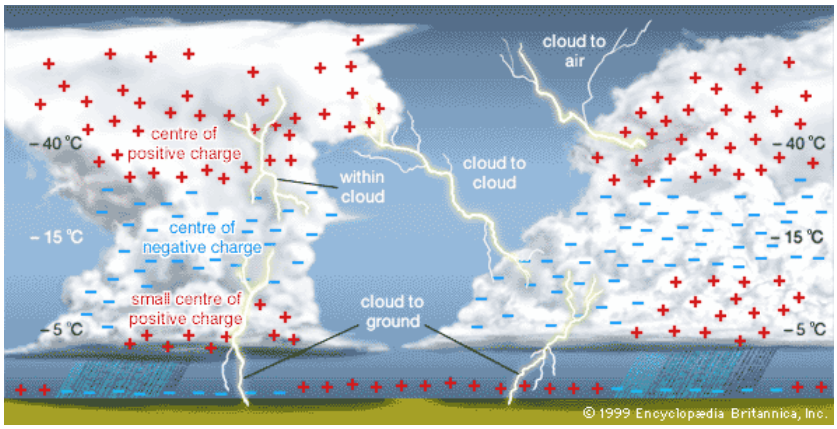

Fig. 2.2: Two thunderclouds with charge distribution and different types of lightning illustrated. Figure from *Dwyer and Uman* [2014].

Lightning is generally separated into the following two categories: cloud-to-ground lightning (CG), which is a discharge between one of the main charge centers of the cloud and the Earth's surface, and lightning that happens entirely in the clouds and air (IC). The latter category includes discharges within one cloud (intracloud), discharges from one cloud to another (intercloud), and cloud-to-air lightning, as seen in Figure 2.2.

While the classical image of a lightning discharge is of the cloud-to-ground variety, IC lightning is in fact much more common. *Boccippio et al.* [2001] found that for a 4-year period the mean IC/CG ratio was 2.94, meaning about 75% of the lightning was intracloud. Due to their location within the cloud cover, IC lightning is also more difficult to detect from the ground.

2.3 Terrestrial Gamma-ray Flashes

Terrestrial gamma-ray flashes (TGFs) are bursts of high energy photons with durations of milliseconds or less. The bursts are bright enough to routinely be observed from spaceborne instruments. Photon energies in TGFs of 20 MeV were observed with the satellite RHESSI by *Smith et al.* [2005], while

the launch of the satellite AGILE lead to reports of photon energies up to 100 MeV [*Tavani et al.*, 2011].

TGFs have been linked to positive intracloud lightning (+IC) [*Stanley et al.*, 2006] where negative charges are transported upward in the cloud. TGF photons are bremsstrahlung from electrons accelerated to large energies by runaway mechanisms within the thunderstorm system. To achieve the photon fluxes that are measured from orbit, the number of such accelerated electrons need to be in the order of 10^{17}. This electron acceleration will be further discussed in the following sections.

2.3.1 Relativistic runaway electrons

When the kinetic energy of an electron in air is sufficiently large, the energy it *gains* from a surrounding electric field will exceed the energy it *loses* in interaction with the air. This causes the electron to gain more and more kinetic energy, and we say that the electron "runs away". This mechanism was first described by *C. T. R. Wilson* [1924].

The energy loss (which is in practice the frictional force on the electron) is shown for different kinetic energies in Figure 2.3. For the runaway mechanism to take place, the electric field needs to be larger than a certain field strength, called the *break-even field*, E_t. The force exerted by this field on the electron corresponds to the lowest point on the frictional force curve in Figure 2.3. To run away, an electron needs an energy above a threshold value of some tens of keV, where the force from the surrounding field intersects the frictional force curve. An electron of such energy is called a *seed electron*. If the electric field is above a critical value, E_c (the peak of the frictional force curve in Figure 2.3), electrons of all energies can run away. This is called *thermal runaway*, and will be discussed further in Section 2.3.4.

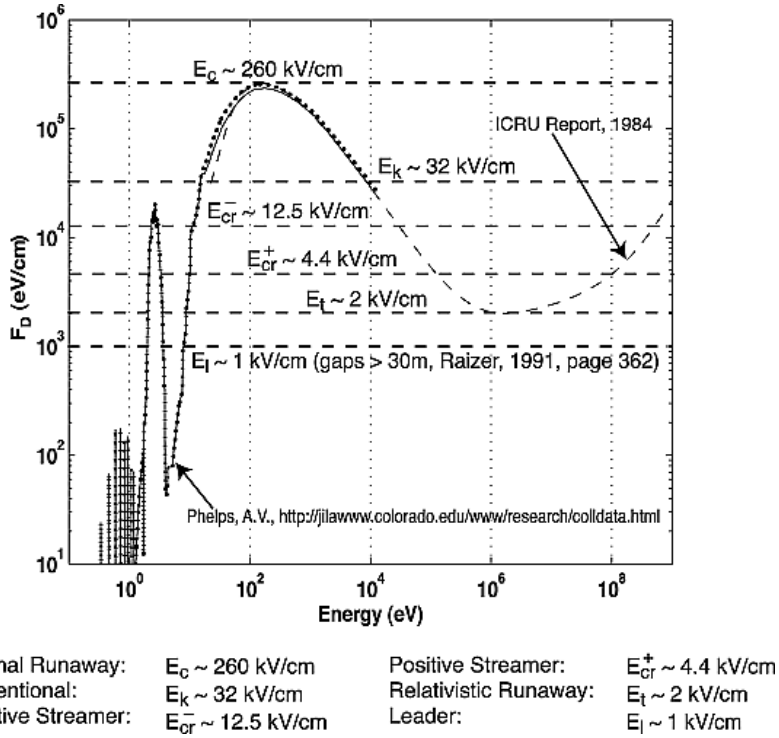

Fig. 2.3: The frictional force on an electron in air, as a function of kinetic energy. Figure from *Moss et al.* [2006].

In the original paper, *Wilson* [1924] suggested that the source of the seed electrons must be cosmic rays or a result of radioactive decay, and that one such particle leads to one runaway electron. By itself, this explanation cannot explain the measured fluxes of X-rays from thunderstorms [*McCarthy and Parks*, 1992].

2.3.2 Relativistic runaway electron avalanches (RREA)

Relativistic runaway electron avalanches (RREA) is a mechanism that can help explain the necessary increase in electron flux. *Gurevich et al.* [1992] proposed that Wilson's runaway electrons paired with electron-electron scattering (Møller scattering) would create an avalanche of relativistic runaway electrons per seed electron that enters an electric field with magnitude larger

than a threshold field. The value of the threshold field, $E_{th} = 2.84 \cdot 10^5 V/m \cdot n$, is slightly higher than the break-down field for classical Wilson runaway electrons, where $E_t = 2.18 \cdot 10^5 V/m \cdot n$ [*Dwyer et al.*, 2012]. The peak values of electric fields in thunderclouds have been measured to be of an equivalent magnitude as the threshold field, E_{th} [*Rakov and Uman*, 2003], [*Marshall et al.*, 1995].

In this scenario, the runaway electron can "knock" an electron off a molecule, and if this knocked-off electron has sufficiently high energy, it can then run away and continue the process. The number of runaway electrons, N_{RREA} is proportional to the number of seed electrons, N_0, and is given by *Dwyer* [2003] as

$$N_{RREA} = N_0 \, e^{L/\lambda} \tag{2.1}$$

with λ being the characteristic length for an avalanche to develop, given by the empirical formula $\lambda = 7200kV \cdot (E - 275kV/M)^{-1}$, and L being the length of the electric field region.

2.3.3 Relativistic feedback

Even taking RREAs into account, the numbers of generated runaway electrons will not be sufficient to explain TGFs. As an addition to the RREA mechanism, *Dwyer* [2003] published the theory of a relativistic feedback mechanism. This mechanism is based on the runaway electrons producing X-rays by bremsstrahlung. Some of these X-rays can travel backwards, back to the source region of the avalanche, and here they might provide new seed electrons for new avalanches through Compton scattering or the photoelectric effect. The X-rays may also pair produce, and the positron travel backwards along the electric field. If the positron returns to the source region, it can scatter electrons that then again might serve as seed electrons for further avalanches. An illustration of the mechanisms can be seen in Figure, 2.4.
Dwyer et al. [2012] gives a feedback factor, γ, which modifies the number of electrons in an avalanche to N_n after n number of avalanche multiplications

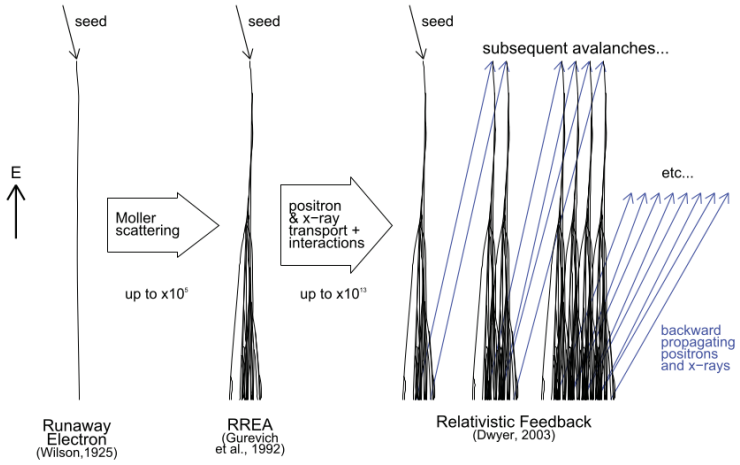

Fig. 2.4: A schematic representation of the mechanisms behind energetic electrons in air with the multiplication factors. Figure from *Dwyer et al.* [2012].

$$N_n = N_{RREA}\ \gamma^n \tag{2.2}$$

with n = 0, 1, 2, ...

The feedback factor is a description of how a RREA relates to the secondary avalannches it causes. This relation can be calculated as the sum of a geometric series, which gives the expression

$$N_n = \frac{N_{RREA}(1-\gamma^n)}{(1-\gamma)} \tag{2.3}$$

Where $\gamma < 1$, the number of electrons will converge towards $N_{RREA}/(1-\gamma)$, increasing the number of electrons from the RREA by a simple factor.

If the feedback factor approaches $\gamma = 1$, the denominator goes rapidly towards zero, and the number of electrons from the relativistic feedback will become much larger than the number stemming from seed electrons.

For $\gamma > 1$, which can happen with a rapid increase of the electric field, the number of electron increases exponentially. This will cause a lot of ionization,

eventually leading the system to produce a discharge current, reducing the electric field [*Dwyer*, 2003], [*Dwyer et al.*, 2012].

2.3.4 Thermal runaway

As an alternative to runaway electrons having to be seeded by cosmic rays or radioactive decay, it is possible for lower energy electrons (thermal electrons) to be accelerated by the high electric fields at the head of streamers. If, in this small area, the electric field exceeds the critical field, E_c in Figure 2.3, thermal electrons can run away. *Celestin and Pasko* [2011] showed that runaway electrons with energies up to $\sim$100 keV could be emitted from the heads of negative streamers. It was also shown that these electrons could be further accelerated by the potential energy of the fields at the tip of the stepped leader. The fluxes of energetic electrons produced by the streamers was high enough to account for satellite measurements of TGFs.

Chapter 3

Discovery and previous observations

3.1 BATSE

The first TGFs were serendipitously discovered by the Burst and Transient Source Experiment (BATSE) aboard the Compton Gamma-Ray Observatory (CGRO). The CGRO launched in 1991 to a low-Earth orbit with an average altitude of 450 km and an inclination of 28.5°. BATSE was designed to detect cosmic gamma-ray bursts — bright flashes of gamma-rays occurring all over the sky with an origin beyond our galaxy [*NASA*, a]. It is an all-sky monitor with eight detectors placed on each corner of the satellite. Because of their arrangement, some detectors are always facing Earth. Events are normally picked up by four of the detectors, which allows directional determination by the relative responses of each detector [*Fishman et al.*, 1989]. By the time the discovery was published by *Fishman et al.* [1994], 12 events of short-duration, hard-spectrum gamma-rays from Earth had been detected, shown in Figure 3.1. During its nine year campaign, BATSE ended up detecting 78 terrestrial gamma-ray flashes [*NASA*, b].

Fishman et al. [1994] noted that the position of the CGRO at the time of the first 12 events was concurrent with areas of high average lightning activity. For seven of the events they also obtained weather images which showed cloud cover with the characteristics of thunderstorm systems. The events are

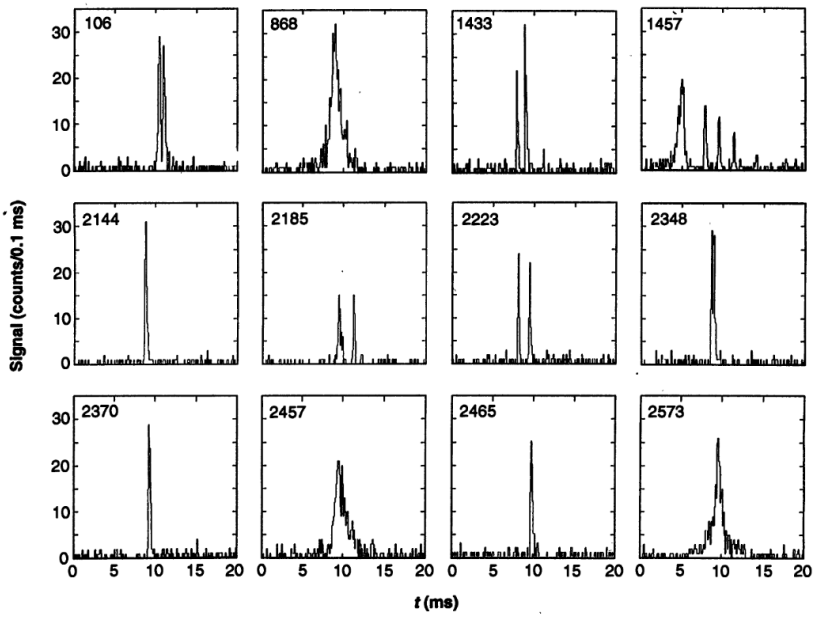

Fig. 3.1: The first 12 TGFs from BATSE. The binsize is 0.1 ms, the width of the peaks ranges from 0.1–2 ms. Figure from *Fishman et al.* [1994]

.

of short duration, 0.1–2 ms, some with more than one peak. The hardness of the spectra were found to be consistent with that of a bremsstrahlung spectrum with a characteristic energy of 1 MeV, and it was proposed that the source of this could be runaway electrons accelerated in the electric fields of thunderclouds.

The BATSE experiment operated in a trigger mode with a minimum sampling time of 64 ms. Because of the short duration of TGFs compared to this window, only very strong events would provide enough gamma-rays to trigger the system [*Fishman et al.*, 1994].

3.2 RHESSI

The Reuven Ramaty High Energy Solar Spectroscopic Imager (RHESSI) was launched by NASA in 2002, and was the second satellite to detect TGFs. As

opposed to BATSE, which only detects in trigger mode, RHESSI detects continuously, registering every photon individually. This makes it possible to search for TGFs that have too short duration or too few counts to trigger BATSE. RHESSI is also able to detect a larger range of energies, from ∼3 keV to ∼20 MeV. Already in the first six months of operation 86 TGFs were identified in RHESSI data, more than BATSE detected during its entire nine year campaign [*Smith et al.*, 2005]. Further description of the RHESSI instrument can be found in Section 4.2.

The TGFs described by *Smith et al.* [2005] were reported to last between 0.2 ms and 3.5 ms, each event containing between 17 and 101 photons. The average duration of the first RHESSI catalog TGFs was later shown to be ∼0.6 ms - 0.7 ms [*Smith et al.*, 2010]. *Dwyer and Smith* [2005] used Monte Carlo simulations to estimate the production altitude of RHESSI TGFs to lie between 15 km and 21 km.

At the time of writing, RHESSI is still operational and detecting new TGFs. The first catalog of RHESSI TGFs was presented by *Grefenstette et al.* [2009], where 820 TGFs were identified between 2002 and 2008. RHESSI's detector sensitivity started declining in 2006 due to radiation damage, but up to this the catalog contains on average one TGF every 2.35 days.

Gjesteland et al. [2012] published a new method of searching the RHESSI data which allowed recognition of fainter events, and for the years 2004–2006 the number of TGFs found with the new method was more than double the number in the first RHESSI catalog. These new events had a slightly softer energy spectrum than the first catalog. This suggests an increased field-of-view, as a larger zenith angle of the gamma-rays is associated with a softening of the observed energy spectrum [*Østgaard et al.*, 2008]. When applied to the years 2002–2013, the method yielded a second RHESSI TGF catalog, containing about 3000 events [*Gjesteland et al.*, 2014].

[*Østgaard et al.*, 2015] further expanded the amount of RHESSI TGFs by superposing data intervals where lightning was detected on Earth within RHESSI's field-of-view. This lead to 141 (or 191, depending on selection criteria) new TGFs distributed over the two years 2006 and 2012. This method will be further explained in Section 5.3, as it is essential to the topic of this thesis.

3.3 Other TGF detections

After the launch of RHESSI several additional instruments capable of TGF detections have come into operation.

3.3.1 AGILE

The Italian satellite Astrorivelatore Gamma a Immagini Leggaro (AGILE) was launched to an orbit with an altitude of 550 km and an inclination of 2.5° in 2007. Its main purpose is gamma-ray astrophysics. One of the onboard instruments, a minicalorimeter (MCAL), detects gamma-rays in the range 300 keV to 100 MeV, and is also able to detect gamma-rays from Earth. Events exhibiting the characteristics of TGFs have been detected since 2007. After improvements of the trigger mechanism in 2008 and 2009 [*Marisaldi et al.*, 2010] and a modification to avoid dead time between triggers in 2015, the satellite was registering more than 90 TGFs per month as of spring 2015 [*Marisaldi et al.*, 2015]. *Tavani et al.* [2011] reported detecting of TGFs with energies up to 100 MeV.

3.3.2 Fermi

The Fermi Gamma-ray Telescope launched in 2008. Like BATSE, its intended purpose was to detect cosmic gamma-ray bursts. Fermi also operates in a trigger mode, but with an accumulation time of 16 ms, much shorter than BATSE's 64 ms. This better facilitates the detection of TGFs [*Dwyer et al.*, 2012]. In 2009 the trigger algorithm was improved, increasing the sensitivity to TGFs tenfold. *Briggs et al.* [2013] estimated that Fermi's Gamma-ray Burst Monitor (GBM) would detect ∼850 TGFs per year with continuous application of the new data acquisition mode.

3.3.3 ADELE

The Airborne Detector for Energetic Lightning Emission (ADELE) is an array of gamma-ray detectors flown by airplane over thunderstorms. In August

and September of 2009 it flew within 10 km of over a thousand lightning discharges. Only one TGF was detected, leading to estimates that 0.1% - 1% of lightning produce TGFs [*Smith et al.*, 2011]. The lack of detection of faint events was reported to speak against a large population of TGFs too weak to be observed from space.

3.3.4 Future missions

ASIM

The Atmosphere-Space Interactions Monitor (ASIM) is an instrument suite designed by ESA to study the effect thunderstorms have on the atmosphere and ionosphere. It will be an externally mounted payload on the International Space Station (ISS). Among its instruments will be cameras, photometers and an X-ray sensor. Its primary observational objectives will include the physics behind TGFs and Transient Luminous Events (TLEs) and the rates with which they occur. [*Neubert et al.*, 2006].

TARANIS

TARANIS is a low altitude microsatellite by the French space agency CNES. It will carry detectors for gamma-rays and energetic electrons, as well as cameras, photometers, magnetometers, and E-field antennas. Its scientific objectives will include the study of TGFs and TLEs , as well as their effects on the atmosphere ans ionosphere [*Pinçon et al.*, 2011].

FEGS

The Fly's Eye GLM Simulator (FEGS) is an airborne instrument by NASA used in preparation of the launch of the Geostationary Lightning Mapper (GLM) onboard the satellite GOES-R. It will fly with an array of telescopes that give a 90° field of view for optical emissions, as well as high energy particle detectors capable of detecting TGFs [*Quick et al.*, 2015].

Chapter 4

Data

In this thesis we use data from two sources. One is a set of the lightning registrations from the World Wide Lightning Location Network (WWLLN) in the period 2002–2015, the other is data from the spectrometer of the satellite Reuven Ramaty High Energy Solar Spectroscopic Imager (RHESSI) from the same period. We only use WWLLN registrations that fall within RHESSI's field-of-view (FOV) of 1000 km from the subsatellite point. This is a total of $1.2 \cdot 10^7$ events, distributed over the years as seen in Table 4.1.

Year	**WWLLN events**	**Year**	**WWLLN events**
2002	116602	2009	919788
2003	91524	2010	1102335
2004	177667	2011	1213982
2005	304345	2012	1518977
2006	400436	2013	1664016
2007	528330	2014	1803725
2008	616474	2015	1830013

Table 4.1: Number of WWLLN registrations within RHESSI's field-of-view in the years 2002–2015.

4.1 WWLLN

4.1.1 Description

Lightning discharges emit radiation in a wide range of frequencies. The World Wide Lightning Location Network (WWLLN) is a network of stations detecting lightning by radio waves in the Very Low Frequency (VLF) range (3–30 kHz). Consisting of more than 70 stations across the world as of 2014, it is estimated to have a global detection efficiency of more than 10%, where strokes with high currents have a significantly larger detection efficiency than those with low currents. WWLLN is also more sensitive to CG than IC lightning, and the detection efficiency of IC was reported by *Abarca et al.* [2010] as only 4.82%. This is worth noting, as TGFs have been connected to positive IC lightning [*Stanley et al.*, 2006].

Fig. 4.1: Geographical location of WWLLN stations as of 2013. Figure adapted from *Mallick et al.* [2014]

.

The number of WWLLN stations worldwide, and thereby its detection efficiency, has been steadily increasing with time. This explains the general increase in lightning per year in Table 4.1. The number of detectors was 18 in 2004, increasing to 30 in 2007, 38 in 2009 and 70 in 2014 [*Abarca et al.*, 2010] [*Mallick et al.*, 2014]. The detection efficiency also varies by geographic area. As an example, at time of writing North America has a much higher detection efficiency than South America, which can be attributed to a higher

detector density, see Figure 4.1. In early years, however, the detection efficiency was much higher in Australia and the Indian Ocean, as this is where the network was started. This can be seen in Figure 4.2, which shows the geographical distribution of all WWLLN registrations within RHESSI's FOV in 2002 versus 2015.

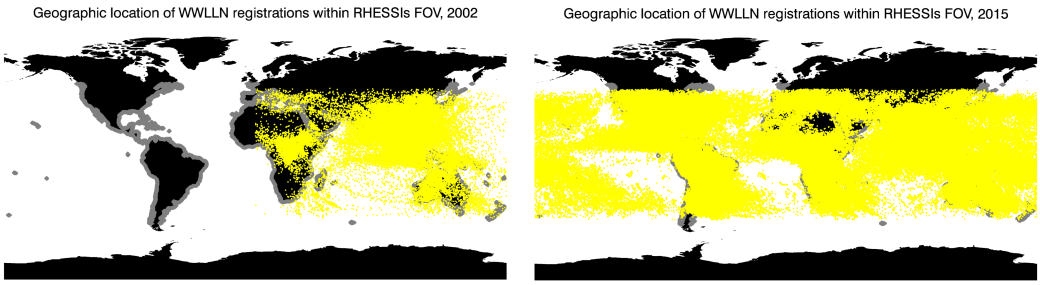

Fig. 4.2: The geographical of all WWLLN registrations (yellow) within RHESSI's field of view in 2002 (left) and 2015 (right).

4.1.2 Lightning location by VLF

The upper layer of the Earth's atmosphere is known as the ionosphere. Ranging from about 60 km to 1000 km, the ionosphere consists of free particles ionized by the Sun's radiation, and thereby acts as a conductive layer. This allows the ionosphere and the Earth's surface to act as a waveguide [*Rakov and Uman*, 2003]. While a wave's power would normally fall off with distance as an inverse square law, a waveguide confines the propagation to one direction, significantly reducing the loss of power.

Lightning discharges emit radiation in a wide range of frequencies. The electric and magnetic fields emitted are often referred to as atmospherics, or just *sferics*. Because of the Earth-ionosphere waveguide (EIWG), these sferics can travel thousands of kilometers. Waves travelling through the EIWG are known as *skywaves*. Because of the longer path, they take longer to travel than waves that propagate along the surface of the Earth (*groundwaves*), which is illustrated in Figure 4.3.

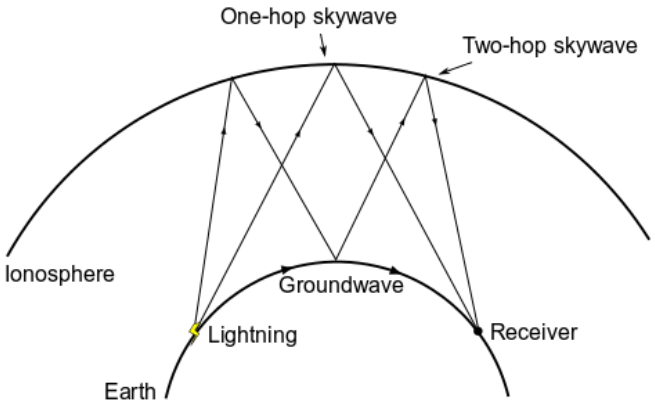

Fig. 4.3: Groundwaves and skywaves in the Earth-ionosphere waveguide. Adapted from *Rakov and Uman* [2003]

.

Some lightning location networks use the difference in time of arrival (TOA) of the wave train from several stations to localize lightning. They operate in the MF band (0.3–3 MHz) and only consider the time where the sharp onset of the groundwave triggers the system. Skywaves, since they arrive slightly later, are not taken into account. While this method seems practical, it requires measuring stations no more than a few hundred kilometers apart in order for the signal, unaided by the EIWG, to be strong enough.

In order to be able to utilize the VLF band, where lightning radiation has the highest power spectral density [*Dowden et al.*, 2002], WWLLN operates by measuring the time of group arrival (TOGA) of the wave train emitted by the lightning discharge. The propagation of waves through the EIWG causes a dispersion of the wave, and there is no clear leading edge of the pulse to give a TOA to trigger detection, see Figure 4.4. A trigger where the amplitude rises above the background can be used, but will cause systematic errors because a strong sferic (having steeper waves) will trigger the system earlier in the waveform than what a weaker sferic would. In stead, the TOGA method uses the whole wave train, and measures the rate of change of the phase with respect to frequency. WWLLN requires the signal to be detected

by five separate stations in order to detect one lightning. [*Dowden et al.*, 2002].

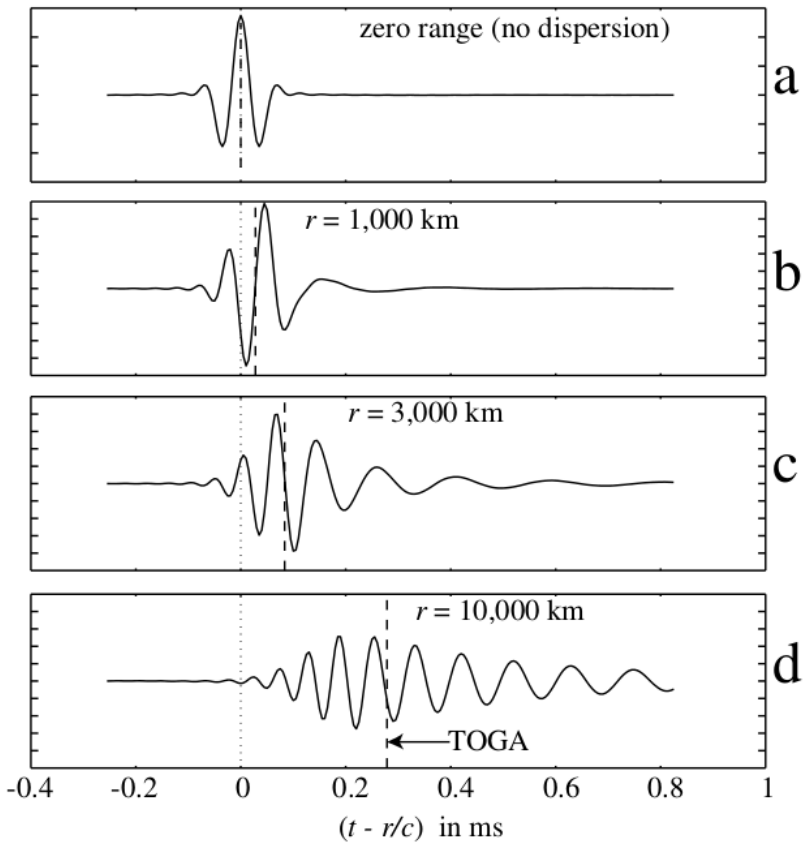

Fig. 4.4: The wave train expanding with distance, r. The time of group arrival (TOGA) is marked with a dashed line. From *Dowden et al.* [2002]

4.2 RHESSI

4.2.1 Description of instrument

The Reuven Ramaty High Energy Solar Spectroscopic Imager (RHESSI) is a satellite which is part of NASA's Small Explorer Mission. It travels spin-stabilized in an orbit of approximately 600 km altitude, with an inclination of 38 degrees. Its original mission is to study solar flares, using an imaging spectrometer [*NASA*, c].

The spectrometer consists of an array of nine cooled germanium crystals, which allows it to detect X-rays and gamma-rays in the energy range 3 keV to 20 MeV. Germanium, when cooled sufficiently, has no electron-hole pairs in the conduction band. An incoming high energetic photon will cause energetic electrons to be released. A strong electric field is applied across the detector, and such released electrons will then create a current pulse proportional to the photon energy [*Smith et al.*, 2002].

Because of the weight restrictions of a Small Explorer mission, RHESSI's detectors are not heavily shielded. This means a significant amount of background is recorded, and in practice makes the instrument an all-sky monitor for X-rays and gamma-rays. Because of its high spectral and temporal resolution, it is also suited as a detector for TGFs [*Lin et al.*, 2002].

4.2.2 Clock error

RHESSI's onboard clock is made to be very precise, down to one binary microsecond (0.9537 μs). However, it suffers from a systematic offset. With the help of TGFs with WWLLN matches, [*Mezentsev et al.*, 2016] determined the timing offset from June 2002 to the end of May 2015, and found that it holds three separate values during this time, as given in Table 4.2.

Period	Offset value
01.06.02 - 05.08.05	-2.359±0.101 ms
05.08.05 - 21.10.13	-1.808±0.050 ms
21.10.13 - 31.05.15	-2.003±0.057 ms

Table 4.2: RHESSI's clock error from 2002–2015. Table adapted from [*Mezentsev et al.*, 2016]

.

4.2.3 Varying background levels

As RHESSI detects on a photon-by-photon basis, it will also detect photons that do not originate from TGFs. Most of this is cosmic radiation and radiation from the Sun. When searching RHESSI's data for TGFs, the radiation from cosmic and solar sources should present as a relatively constant background level, with the exception of certain events such as solar flares and cosmic gamma-ray bursts. The background radiation acts as noise, obscuring the signal of the TGFs, and when working with weak events one of the main challenges is separating the signal from the background noise.

If RHESSI's onboard memory starts filling up, a process known as *decimation* will only keep 1/N of detected energies below a threshold energy. N can vary from 2 to 16, and the threshold energy from 150 keV to 450 keV [*Smith et al.*, 2002].

The South Atlantic Anomaly

The South Atlantic Anomaly (SAA) is an area of increased flux of energetic particles, caused by the assymmetry of the geomagnetic field. RHESSI passes through this area about 5 times a day, and is turned off as it goes through [*Lin et al.*, 2002]. This area is where the majority of radiation damage to the detectors happen.

Annealing

Without any heavy shielding, RHESSI's germanium detectors suffer radiation damage, and the energy resolution deteriorates over time. The major part of this damage is due to protons, mostly encountered in the SAA, being caught in the crystal lattice, causing disordered regions. This can be reverted by a process known as *annealing*, where heating the crystals removes most of the damage. To date, RHESSI has been annealed five times, in 2007, 2010, 2012, 2014, and 2016. The instrument is switched off for about a month when the procedure takes place [*Smith et al.*, 2002], [*NASA*, d].

Chapter 5

Method

As a way of identifying TGFs that were not picked up by the algorithms of *Grefenstette et al.* [2009] and *Gjesteland et al.* [2012], *Østgaard et al.* [2015] developed a method of superposing RHESSI data intervals centered around the times where WWLLN detects lightning within RHESSI's field-of-view. This method involves selecting the appropriate WWLLN detections within 1000 km of RHESSI's subsatellite point, and calculate the propagation of the signal from the lightning to RHESSI.

Østgaard et al. [2015] only had the years 2006 and 2012 available to them. This thesis will expand on their work, using all years from 2002 to 2015. This chapter will describe the methodology used in the process of searching for TGFs with the help of superposed data strings, as well as describe the method we later use to place TGFs in geographical zones.

5.1 Calculating RHESSI's position and timing

When matching WWLLN-observations with RHESSI data, one has to account for the propagation time of the gamma-rays over distance between the lightning and the satellite.

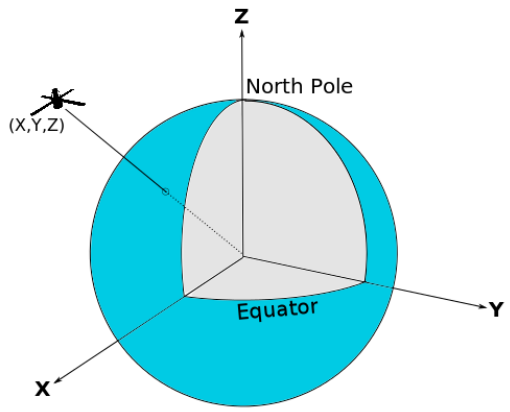

Fig. 5.1: The Earth Centered Inertial (ECI) coordinate system. It is centered in the center of the Earth, the x-axis is fixed with respect to the celestial sphere, the Earth's equatorial plane lies in the x-y-plane, and the z-axis extends through the poles.

First one needs to extrapolate RHESSI's position $(x_{RHESSI}, y_{RHESSI}, z_{RHESSI})$ at the exact moment of the lightning WWLLN has registered, t_{WWLLN}. RHESSI sends its position and velocity data in x-, y-, z-components only every 20 seconds, so one can do a linear extrapolation from the last known data point (x_0, y_0, z_0) by adding $\triangle$t times velocity (v_x, v_y, v_z) to the position for each of the three components. $\triangle$t being the time elapsed since last known position. The position is given in the middle of the 20 second interval, so 10 seconds (half the interval) have to be added to the time you get from RHESSI.

$$\begin{aligned} \triangle t &= t_{WWLLN} - (\text{time you get from RHESSI} + 10\text{s}) \\ x_{RHESSI} &= x_0 + v_x \cdot \triangle t \\ y_{RHESSI} &= y_0 + y_x \cdot \triangle t \\ z_{RHESSI} &= z_0 + z_x \cdot \triangle t \end{aligned} \tag{5.1}$$

We then calculate the distance between RHESSI and the WWLLN-observation by the Pythagorean theorem. This is easier to do in Earth Centered Inertial (ECI) coordinates than latitude and longitude, see Figure 5.1, so this is what is used here.

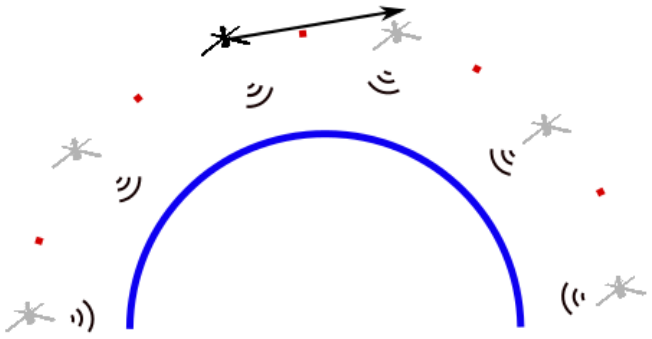

Fig. 5.2: RHESSI transmits position and velocity every 20 seconds, giving the position in the middle of the 20 second interval (red dots). We extrapolate RHESSI's position between each transfer point as a straight line.

$$distance = \sqrt{(x_{RHESSI} - x_{WWLLN})^2 + (y_{RHESSI} - y_{WWLLN})^2 + (z_{RHESSI} - z_{WWLLN})^2} \tag{5.2}$$

The propagation time, $t_{propagation}$, of the gamma rays is this distance divided by the speed of light, c.

$$t_{propagation} = distance/c \tag{5.3}$$

Then we correct the WWLLN-time for this and for RHESSI's clock error (see Section 4.2.2), and end up with the time where RHESSI should register the signal, t_{RHESSI}.

$$t_{RHESSI} = t_{WWLLN} + t_{propagation} \text{- clock error} \tag{5.4}$$

5.1.1 Uncertainties in timing and position

The main source of uncertainty when calculating the propagation of the signal comes from WWLLN's positional uncertainty of 15 km [*Østgaard et al.*, 2013].

The largest possible error we can get from this is when using a maximum distance of 1000 km from the subsatellite point. This could then increase the real arc length (distance along the Earth's surface) to 1015 km.

From the arc length, we can find the angle θ, seen in Figure 5.3, in radians by the relation $\theta = s/R_E$, where R_E is the radius of the Earth. This allows us to use the law of cosines on the triangle in Figure 5.3 to solve for the distance d from the lightning to RHESSI.

Doing this for s = 1000 km and s = 1050 km yields a difference in distance, d, of $\triangle d = 14.2$ km. Assuming the signal travels at the speed of light, this corresponds to a timing uncertainty of 47.3 μs.

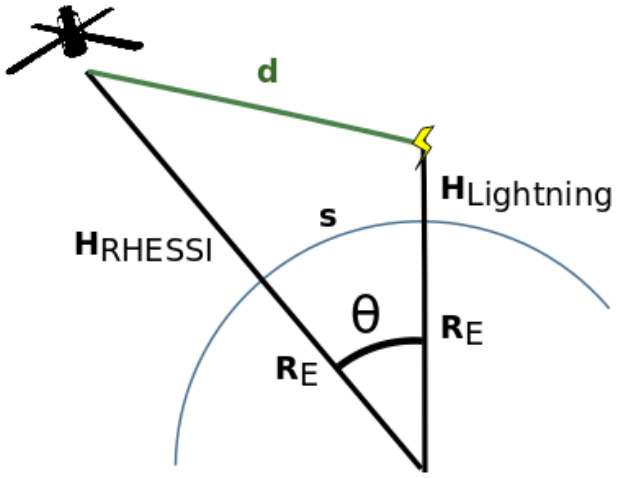

Fig. 5.3: Illustration of the distance, d, that the signal from the WWLLN registrations has to travel to reach RHESSI. R_E is the Earth's radius, H_{RHESSI} and $H_{Lightning}$ are the altitude of RHESSI and production altitude of lightning, respectively.

Other sources of uncertainty in propagation timing

Throughout this thesis we have used 15 km as the production altitude of lightning. *Dwyer and Smith* [2005] cites the production height to be between 15 km and 21 km, giving a maximum error of 6 km. This error is however

much smaller than the one from WWLLN's location. The two errors are also correlated — the altitude error gives the largest impact on the propagation calculation at the subsatellite point, while the WWLLN location uncertainty matters most at maximum distance from this point.

RHESSI also moves during the time of signal propagation. However, during the $\sim 4 \cdot 10^{-3}$ seconds the signal uses from a distance of 1000 km from the subsatellite point, RHESSI will only have moved ∼30 m at its speed of about 7600 m/s. We consider this to be negligible.

Uncertainty of linear extrapolation of position

As can be seen in Figure 5.2, the linear extrapolation of RHESSI's orbit between transmissions leads to an error of position, largest at the point right before the next transmission. RHESSI's speed of about 7600 m/s leads to a distance of d = $1.52 \cdot 10^5$ m traveled in the 20 second window. For an equal arc length, s, it is then possible to calculate the difference in distance between a circular path and the linear extrapolation, $\triangle d$, see Figure 5.4. We find the value of $\triangle d$ to be 1661.4 m, corresponding to a maximum timing difference of ∼5.5 μs, which is small enough to be negligible in comparison to other uncertainties.

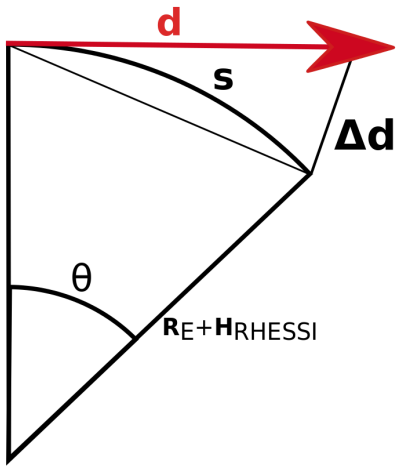

Fig. 5.4: The linearly extrapolated path of RHESSI between position transmissions (red), with the corresponding arc length, s, of a circular path in black. R_E is the Earth's radius, H_{RHESSI} is RHESSI's altitude.

5.2 Filtering the data

After matching the WWLLN times with the RHESSI measurements, there is a final filtering of the data, in order to exclude spurious events.

- **Distance from subsatellite point**

  Since the strength of the signal from a TGF decreases with distance due to attenuation in the atmosphere, excluding all events from outside a certain radius from RHESSI's subsatellite point can give a better signal-to-noise ratio. To find which radius is optimal to use is one of the objectives that will be discussed in Section 6.1.

- **High background and empty event lists**

  When RHESSI travels through the SAA, the instrument is turned off. This gives periods of times with no telemetry data. These are removed to avoid skewing the results.

  Events with abnormally high background levels have also been removed, as they are thought to be caused by other factors than TGFs, such as

solar flares or the Earth's radiation belts. Very high count rates can also appear just as the instrument is turned back on after annealings. Such instances can affect the mean values and are therefore removed. From the distribution of the background level, seen in Figure 6.2, the cut-off is chosen to be events with more than 400 counts per 100 ms.

- **Multiple events within one binsize**

  For instances where there are multiple lightning detections within the time interval we use as a binsize later, the duplicates are removed. This is because the photon counts from all such events will already have been accounted for in the first string of RHESSI data extracted.

- **Event lists with large empty holes**

  In order to avoid incomplete strings of data skewing or otherwise corrupting the results, strings with holes of more than 20 ms with no detection are removed. Assuming Poisson statistics, the probability of 20 ms without detection is given by

$$P(k\ events\ in\ interval) = e^{-\lambda}\frac{\lambda^k}{k!} \tag{5.5}$$

  Where λ is the mean number of counts per interval. In Section 6.1, we find the mean to be $\lambda = 0.33$ per binsize of 250 μs. The probability of a 20 ms hole is then P(20 ms hole) = p(0 events in 250 μs)^{80} = 3.42·10^{-12}, which should be an acceptably low chance of wrongfully removing an actual event in order to avoid including incomplete strings.

5.3 Superposing data intervals

When searching for TGFs with weak signal strengths, we encounter the problem that each single event may not be clearly distinguishable from the background level. In order to achieve a statistically significant result, we can superpose strings of RHESSI data. The string is centered around the exact time where gamma-rays from a WWLLN lightning should reach RHESSI, taking propagation time and the RHESSI clock error into account. The data strings are, as shown in Figure 5.5, histograms of the number of counts per

time. The superposing of the strings simply involves adding the histograms together. This method is based on the work by *Østgaard et al.* [2015], and similar methods have previously been used by *McTague et al.* [2015] and *Smith et al.* [2016] with varying results.

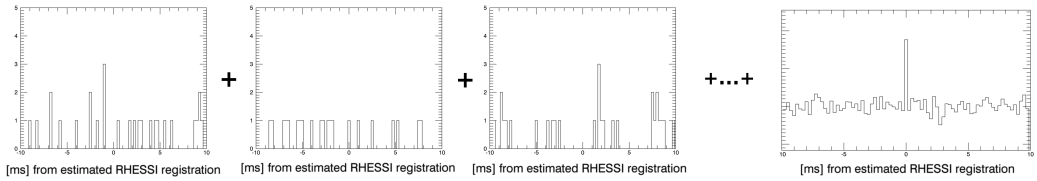

Fig. 5.5: Superposing strings of RHESSI data. To the left are individual data intervals centered around the time where photons originating from a WWLLN lightning would arrive. To the right is the result of adding all strings from 2002 to 2015.

As can be seen from Figure 5.5, the strings of data that are added together do not necessarily have any form of peak, in fact the vast majority do not. However, when we superpose the strings of all the WWLLN registrations that are left after the initial filtering, we get a significant signal. The results will be more thoroughly discussed in Section 6.1.

5.4 Geographical distribution of TGFs.

One of the goals of this thesis is to examine the geographical distribution of the TGFs we find. The method developed for determining whether WWLLN registrations fall over ocean or land is presented here. The motivations and results will be further discussed in Section 6.3.

In order to avoid ambiguous situations where a thundercloud system is partially above land and partially above ocean, we have also added a coastal zone. We set the radius of this zone as 150 km. This is based on small thunderstorm having a radius of 6–10 km, and large systems of storms sometimes being hundredfold as large in area, meaning a radius in the order of 100 km [*Dwyer and Uman*, 2014]. A radius of 150 km should then be on the safe side, even for larger storms, while also taking into account WWLLN's

position uncertainty of 15 km [*Østgaard et al.*, 2013]. There are even larger storm systems that can occur, but these are rare, and the trade-off of using the upper bound values as the coastal zone would be to turn the entire Caribbean and Indian oceans into coast.

To be able to identify where on the map a WWLLN registration falls, we turned a high resolution black-and-white map with filled-in landmass into a binary array. The resolution is ten pixels per degree. In order to make the coastline, we created a similar array created from a map with only the landmass outlines. We added an approximation of a circle with the radius of the extent of the coastal zone to each pixel of coast in the latitude range of RHESSI's field-of-view. We adjust the circle approximation into an elliptical approximation with latitude, taking into account the narrowing of the distance between 1° longitude lines when moving towards the poles. We combined these two binary arrays to an array with three number values for the three zones ocean, land and coast. By converting the geographical coordinates of the WWLLN registrations into the corresponding array indexes, we can then place the lightning to a tenth of a degree's accuracy.

Lay et al. [2007] made a similar geographical distribution of WWLLN registrations when evaluating WWLLN's detection efficiency. *Lay et al.* [2007] used data from 2003-2005, and used a 600 km coastal zone, defined by the FOV of a satellite they were using. As such, the numbers they got were different from the ones we will present later (see Section 6.3), but are useful as a guide to validate our numbers. The percentage of events in the *Lay et al.* [2007] paper for ocean, coast, and land, were 7.8%, 81,24%, and 10.9%, respectively. Using our method for the year 2003, changing the coastal radius to 600 km, we get 10.0%, 79.6%, and 10.4%, correspondingly. Considering we are limiting ourselves to WWLLN registrations within RHESSI's FOV,and also using data from only one of the years, we cannot expect the results to be entirely identical. We therefore find these numbers to be acceptably close.

Chapter 6

Results and discussion

In this chapter we will present results of three main topics of this thesis — the optimization if selection criteria for weak TGFs, and a study of the variation in RHESSI's background levels, and the TGFs' geographical distribution.

Because the three sections are relatively independent, each section's results will be both presented and discussed within this chapter. This is to allow continuity of thought for the reader.

6.1 Optimization of selection criteria

When searching for weak signal TGFs from WWLLN lightning detections, there are two main parameters that need to be defined — the distance from the lightning to RHESSI's subsatellite point, and the binsize we use when superposing strings of RHESSI registrations. For further use of the data we also need to define the minimum amount of counts which we categorize as a potential TGF.

When searching for WWLLN registrations within RHESSI's field-of-view, we define a maximum radius from the subsatellite point. This area will necessarily increase as the square of this radius, and so will presumably the average number of WWLLN detections found in the area. A greater number of WWLLN detections gives us more data to use, but with the trade-off

that any potential TGF's signal will be weaker the further away it originated. By increasing the radius too much, we can therefore risk including only background, thus decreasing the overall signal-to-noise ratio.

As seen in Section 4.2.2, RHESSI's clock has a maximum uncertainty of 101 μs. Together with the WWLLN's timing uncertainty of 45 μs [*Østgaard et al.*, 2013], and the error of propagation calculation (47.3 μs, see Section 5.1.1) this makes up the main time uncertainties. These three uncertainties are uncorrelated, and should be added in quadrature, which yields a timing uncertainty, Δt, of

$$\triangle t = \sqrt{(101\mu s)^2 + (47.3\mu s)^2 + (45\mu s^2)} = 120.3\ \mu s \tag{6.1}$$

meaning that any binsize used should be larger than this.

TGF durations range from about 0.1 ms to 1 ms. For the first RHESSI catalogue TGFs the average duration was reported as ∼0.6 ms–0.7 ms by *Smith et al.* [2010], while *Briggs et al.* [2013] reports a median of 240±25 μs for Fermi TGFs. A too small binsize will cause counts to fall outside the center bin, while too large a binsize will include more background. This will decrease the signal-to-noise ratio, as the noise rises but the signal would stay constant.

In order to find the optimal combination of these two parameters, we have performed a calculation of how many standard deviations, σ, the peak rises above the background level when superposing light curves at the time of WWLLN registrations from 2002 to 2015. Assuming Poisson statistics, the standard deviation is given by $\sigma = \sqrt{\lambda}$, where λ is the mean number of background counts per bin. The results can be seen in Table 6.1.

μs km	700	750	800	850	900	950	1000
200	10.68σ	10.78σ	10.86σ	10.93σ	10.96σ	10.69σ	10.20σ
250	11.19σ	11.10σ	11.17σ	11.45σ	**11.48**σ	11.22σ	10.67σ
300	10.25σ	10.00σ	9.93σ	10.03σ	9.94σ	9.76σ	9.44σ
350	9.82σ	9.45σ	9.52σ	9.51σ	9.32σ	9.37σ	9.41σ
400	9.26σ	8.90σ	8.94σ	8.81σ	8.90σ	8.71σ	8.79σ

Table 6.1: Sigma for varying distance from subsatellite point and binsize

As can be seen, the σ-values peak at the binsize 250 μs, with the radius 900 km having the highest sigma value for this binsize. The histogram of the superposed RHESSI data can vbe seen in Figure 6.1 and the background distribution for these values in Figure 6.2. The mean value of the background is 0.33 counts per bin of 250 μs.

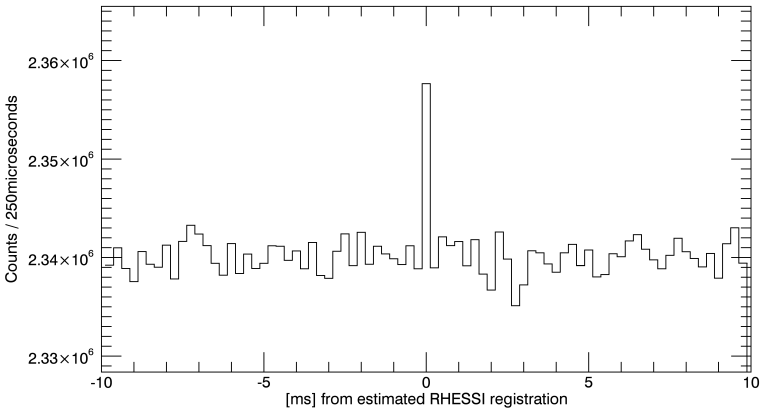

Fig. 6.1: Result of superposing RHESSI data corresponding to WWLLN registrations with maximum distance from subsatellite point of 900 km, with a binsize of 250 μs. TGFs in the *Gjesteland et al.* [2012] catalog are removed.

6.1.1 Finding potential TGFs

Having done the superposition of data strings, as seen in Figure 6.1, we can clearly see that some events have caused a peak, and due to their perfectly aligned timing, we must assume that these events are in fact TGFs. The challenge remains to sort these potential TGFs out from all the events with no signal. To do so we start with plotting a histogram distribution of the number of counts the peak bin contains for each single event.

We also add the same plot for the average of a sample of the background bins, as well as the probability for each number value given that the counts happen as a Poisson distribution. The background sample is made from 40 bins, in intervals of 20 bins on each side of the peak. These two background

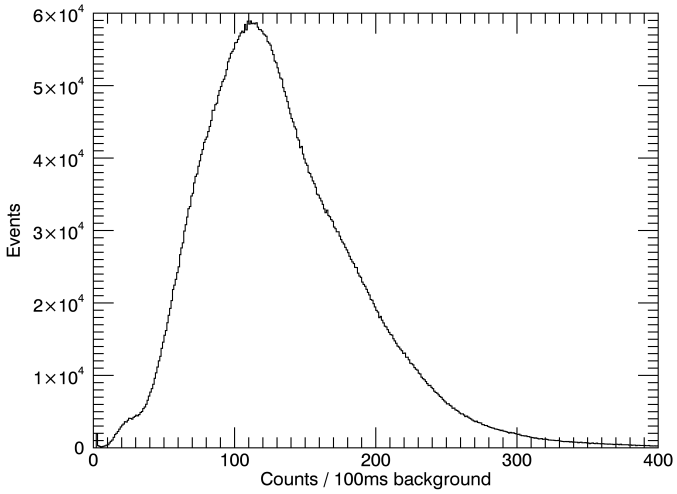

Fig. 6.2: RHESSI's background distribution at times corresponding to WWLLN registrations with maximum distance from subsatellite point of 900 km, and a binsize of 250 μs.

intervals are chosen as $\pm 9\ ms \mp 20 \cdot binsize$ with the peak in Figure 6.1 at time 0. The Poisson probability is given by

$$P(k\ events\ in\ interval) = e^{-\lambda} \cdot (\lambda^k / k!) \tag{6.2}$$

where λ is the mean per interval corresponding to the chosen binsize, and k is the number of counts. Noting the logarithmic y-axis of Figure 6.3, we can see that the peak counts start significantly surpassing the background at five counts. The figure also shows that the background does not follow the Poisson distribution, but rather has more counts at higher values. This will be discussed further in Section 6.2.

The numbers of the counts in the peak over counts in background can be seen in Table 6.2. The table shows how many times the peak and the background has exceeded different numbers of counts in the 14 years of WWLLN registrations we use. The percentage given is a measure of how much of the peak that rises above the background, and is given by

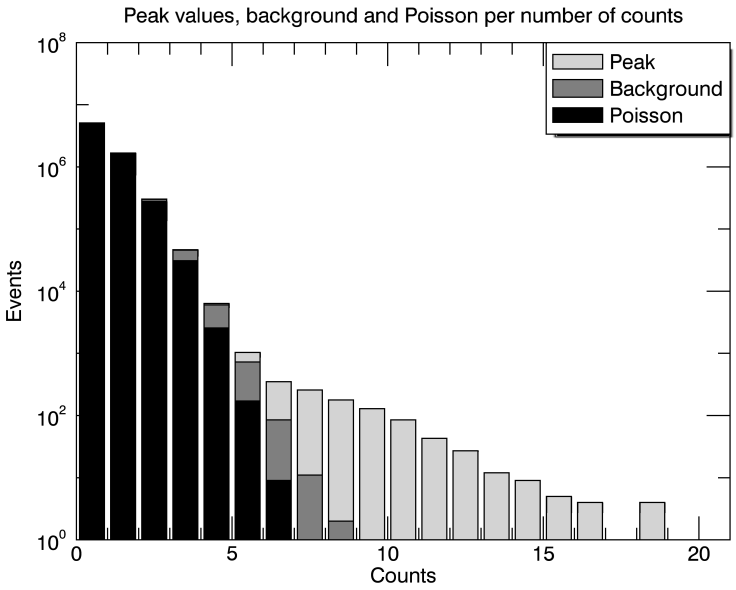

Fig. 6.3: Distribution of peak values, background and Poisson probability per number of counts, after removing TGFs from the *Gjesteland et al.* [2012] catalog.

$$percentage = (peak - background)/peak \cdot 100 \tag{6.3}$$

What to use as the minimum value of peak counts that we accept as a TGF for further study, depends on the certainty required. For the combination of a radius of 900 km and a binsize of 250 μs which gave the best sigma value in Table 6.1, a minimum of seven counts gives a high certainty with 755 events and only 13 suspected background events included (see Table 6.2). A minimum of six counts gives 240 more probable actual TGFs to work with, but also includes more suspected background. We note the added uncertainty, but will choose six as the minimum amount of counts for further use.

In Figure 6.4, we can see the distribution of the distance to RHESSI's sub-satellite point of the events with six counts or more. We can see how the number of events falls off with distance, which validates the assumption that

	$\geq$ **5 counts**	$\geq$ **6 counts**	$\geq$ **7 counts**
Peak/background	2138/825	1106/98	755/13
Percentage	61.41%	91.14%	98.28%

Table 6.2: Peak and background occurrences for different number of counts.

including events further out leads to a reduced signal-to-noise ratio. Superposed in green is the same distribution for the TGFs in the Gjesteland catalog with WWLLN matches. The Gjesteland distribution is scaled to contain the same number of events as the new distribution to ease comparison.

As we can see, the new TGFs are more likely to be found further away from the subsatellite point. The mean distance from subsatellite point of the Gjesteland TGFs is 333.3 km, while for the new TGFs the mean is 408.3 km. That our new population of weak signal TGFs tends to be further from the subsatellite point makes sense, as we expect the intensity of TGF signals to fall of with distance, and when propagating through the atmosphere.

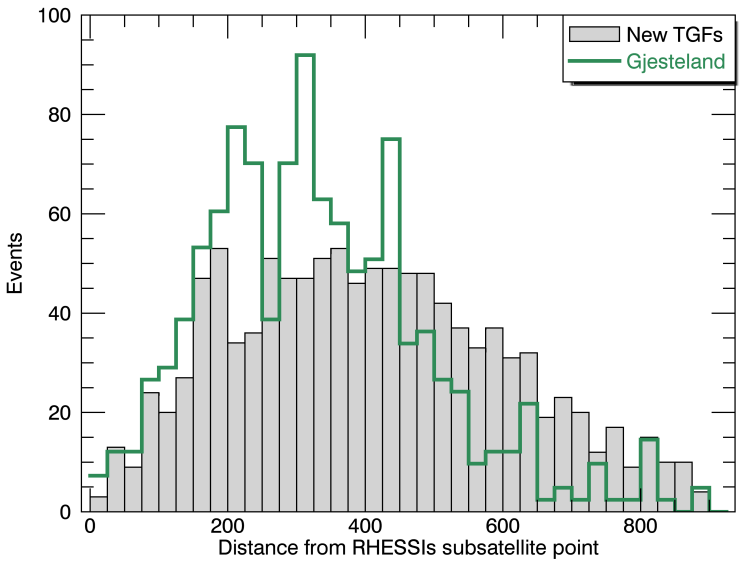

Fig. 6.4: Distribution of distance to subsatellite point, for events with six of more counts in the center bin. The same distribution for is outlined in green for TGFs with WWLLN matches from the Gjesteland catalog. To ease comparison, the Gjesteland distribution is scaled to contain the same number of events as the new distribution.

6.2 Background levels

The background distribution we saw in Figure 6.2 is considerably wider than a Poisson distribution with the same number of events around the same mean, as can be seen in Figure 6.5. In this section we will investigate some of the effects that might cause the widening of the background distribution.

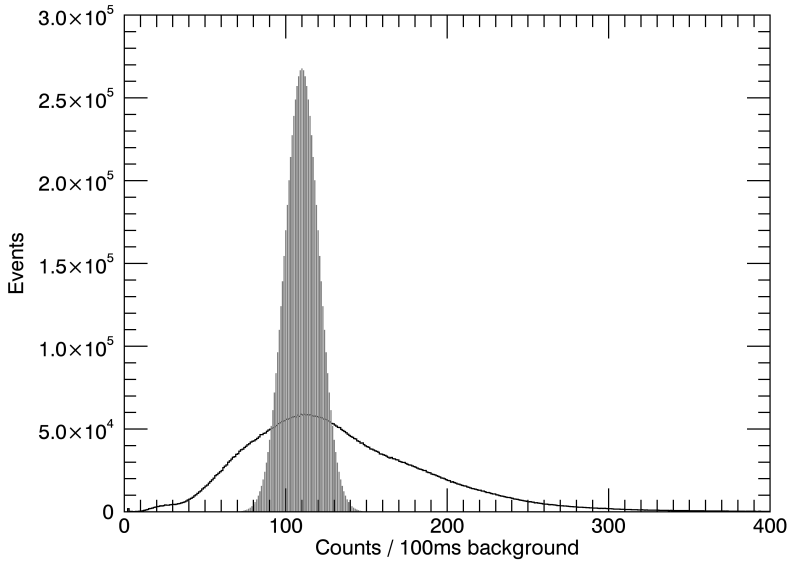

Fig. 6.5: Observed background distribution (black line) and calculated Poisson distribution (grey) for an equal number of events around the same mean.

6.2.1 Variation after annealings

As described in Section 4.2, RHESSI's detectors constantly suffer radiation damage. In order to reverse this, the instrument is annealed. The decreased detector sensitivity due to damage and subsequent increased sensitivity after annealings cause the average background level to vary. In Figure 6.6, we can see this effect taking place before and after the 2012 annealing. Right before the annealing the background is low, only at about 100 counts per 100 ms, and right after it has increased to about 200 counts per 100 ms. After this, we can see a steady decline which will continue until the next annealing.

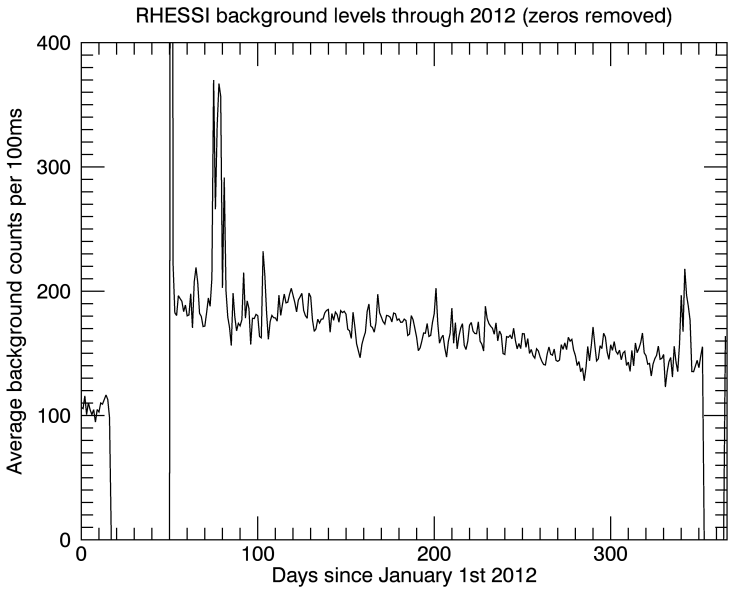

Fig. 6.6: RHESSI's background levels around time of annealing.

6.2.2 Magnetic latitudes

Distribution per magnetic latitude

Another factor contributing to the widening of the background distribution could be that RHESSI travels through different magnetic latitudes. The Earth's magnetic field generally provides better protection against incoming radiation at the equator, and less protection towards the poles.

To study this we plotted the background distribution for different ranges of magnetic latitude. The result can be seen in Figure 6.7. There are noticeably fewer events at southern latitudes, which is easily explained by the fact that RHESSI's detectors are shut off during its transit through the SAA. The northern latitudes contain more events, and counter-intuitively seem to peak at lower values than the total mean.

Other than this, it is not easy to tell much from this plot. Each of the latitude ranges has a slightly narrower distribution than the total, but not enough to

give a full explanation of the wideness of the total distribution.

To eliminate the changes in background level due to detector sensitivity over the years, we also did the same plot for a three week period starting June 5th 2012. This period was chosen because it is relatively shortly after an annealing, and the background level in this period seems pretty consistent. It is located around day 170 in Figure 6.6, where the count rate is relatively flat. The results can be seen in Figure 6.8. Here it is difficult to tell anything from the southern latitudes because of the low number of events in each latitude range, but for the northern latitudes the full width at half maximum is considerably narrower than that of the total distribution. Especially the latitude interval 30–35°N seems to approach a Poisson distribution.

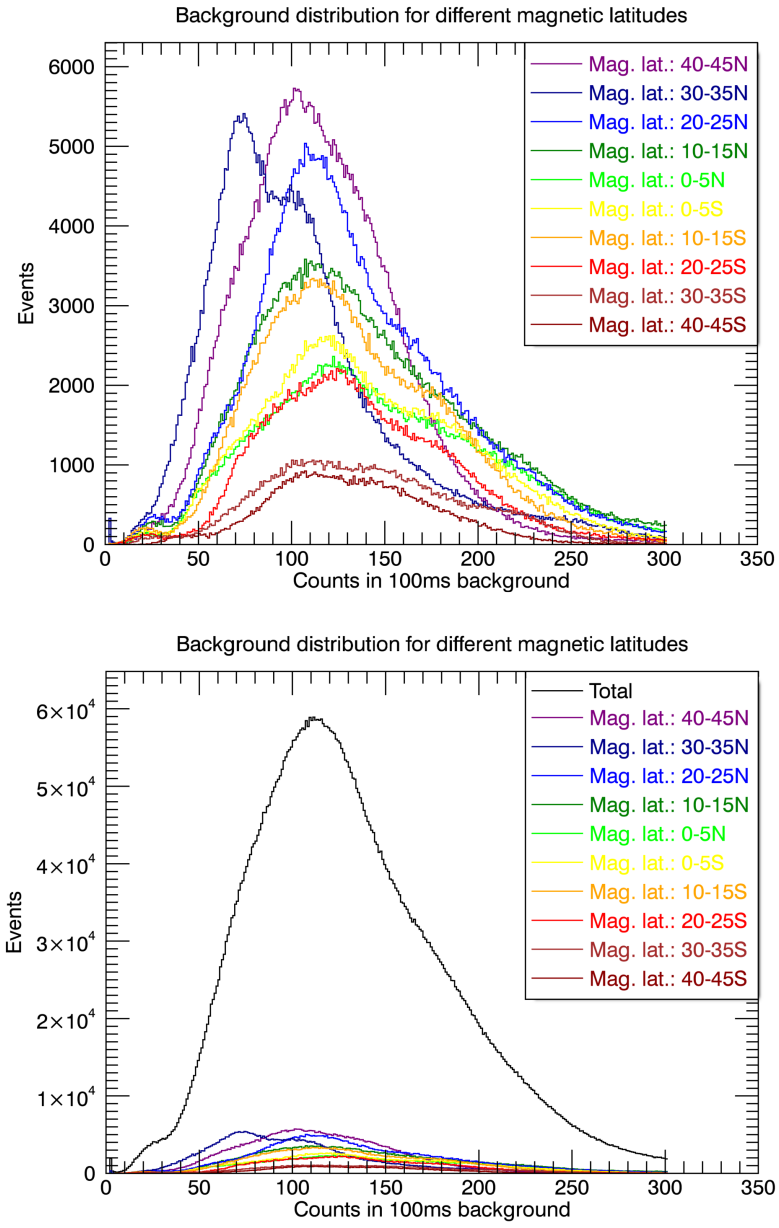

Fig. 6.7: Background distributions for selected magnetic latitudes (top), and with the total distribution across all latitudes added (bottom). RHESSI data read at the points of WWLLN registrations within its field of view 2002–2015.

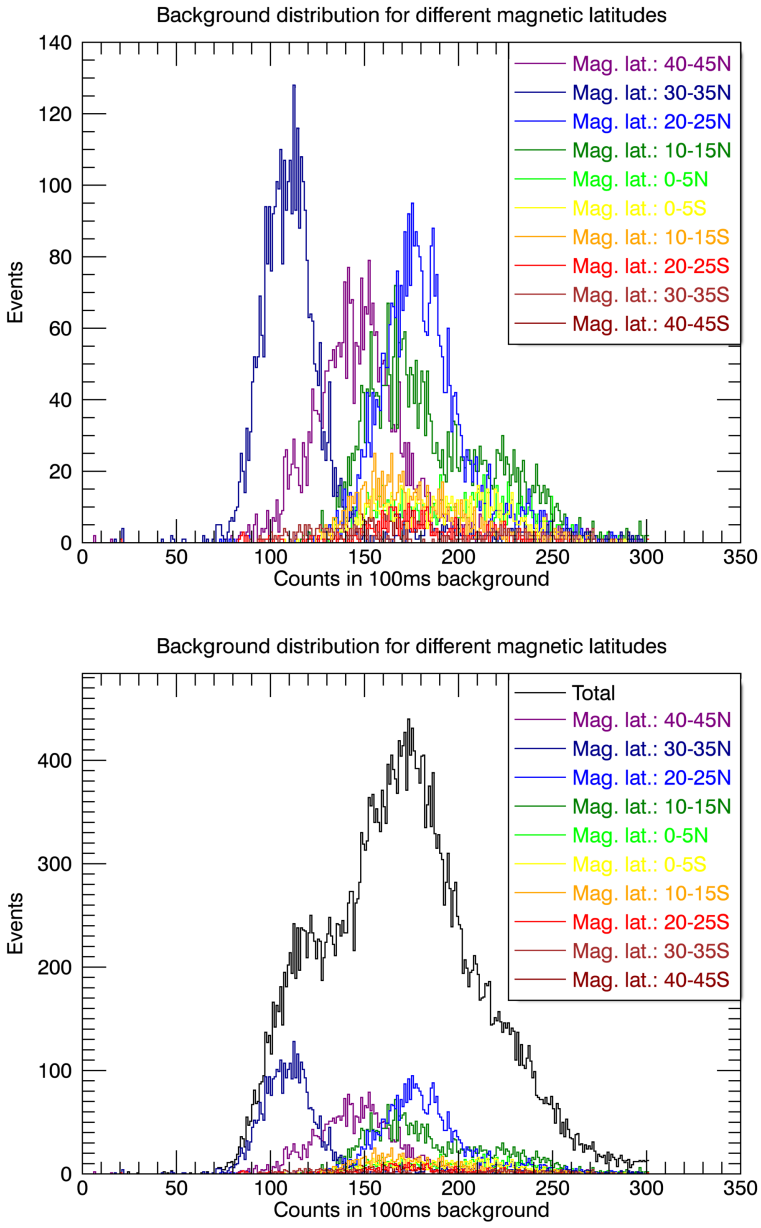

Fig. 6.8: Background distributions for selected magnetic latitudes (top), and with the total distribution across all latitudes added (bottom). RHESSI data read at the points of WWLLN registrations within its field of view 5th–26th of June 2012.

Single orbits

To further investigate the change of the background level with magnetic latitude, we investigated how the background levels change through single half-orbits of RHESSI. Starting at a maximum or minimum latitude, we extracted a string of background once every minute for the 48 minutes it takes RHESSI to complete half an orbit around the Earth. The orbits were always chosen so as not to include transits through the SAA.

One such half orbit is presented in Figure 6.9. This orbit is picked from the same period of June 2012 that was used in the previous section. Here we can see the expected shape of higher background levels at higher latitudes (the absolute value of the latitude is in red at the bottom of the plot). There are however three instances where the background level drops dramatically. It is also worth noting that the background here averages almost 300 counts per 100 ms, which is much higher than the average of the background distribution seen in Figure 6.2.

This predicted shape is however not always the case. In Figure 6.10, we see a randomly chosen orbit from 2014. Only small parts of the orbit seem to follow the expected pattern in background, if it can be said that it is followed at all. It is however worth noting that the average number of counts per 100 ms seems much more representative.

This brings us to the conclusion that there must be effects that affect the background level more than the magnetic latitude does. Upon further investigation, we found the reason for the deviation from the expected variation with magnetic latitude. As described in Section 4.2.3, RHESSI starts a process known as *decimation* when its onboard memory is in danger of filling up. This involves that under a certain energy threshold, varying from 150 keV to 450 keV, only a fraction of events are saved [*Smith et al.*, 2002].

As can be seen in both Figure 6.9 and Figure 6.10, decimation is active at times exactly corresponding with the background's deviation from the expected pattern. In both cases the decimation is in RHESSI's rear segments.

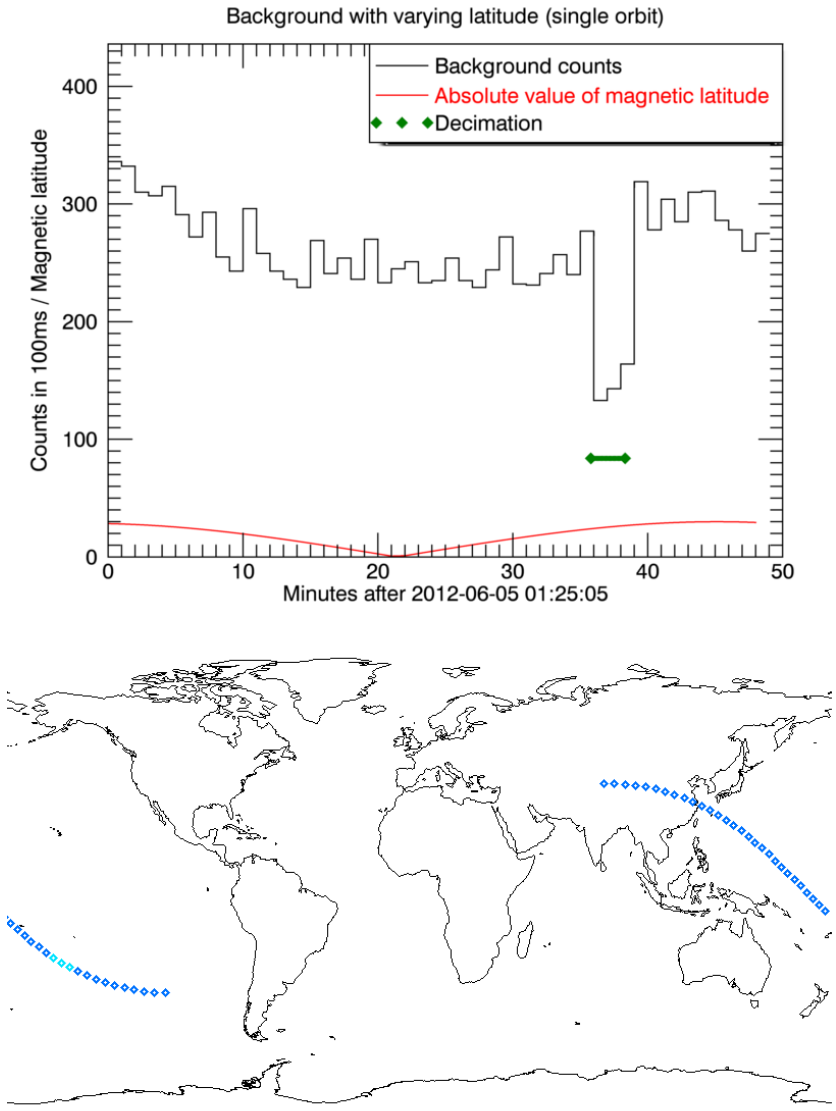

Fig. 6.9: Counts in 100 ms background for varying magnetic latitude in the course of one half-orbit of RHESSI. The absolute value of the magnetic latitude is shown in red, and times decimation is active is shown in dark green. The geographic location of the orbit can be seen on the bottom. The positions corresponding to bins with less than 200 counts are marked in lighter blue for visibility.

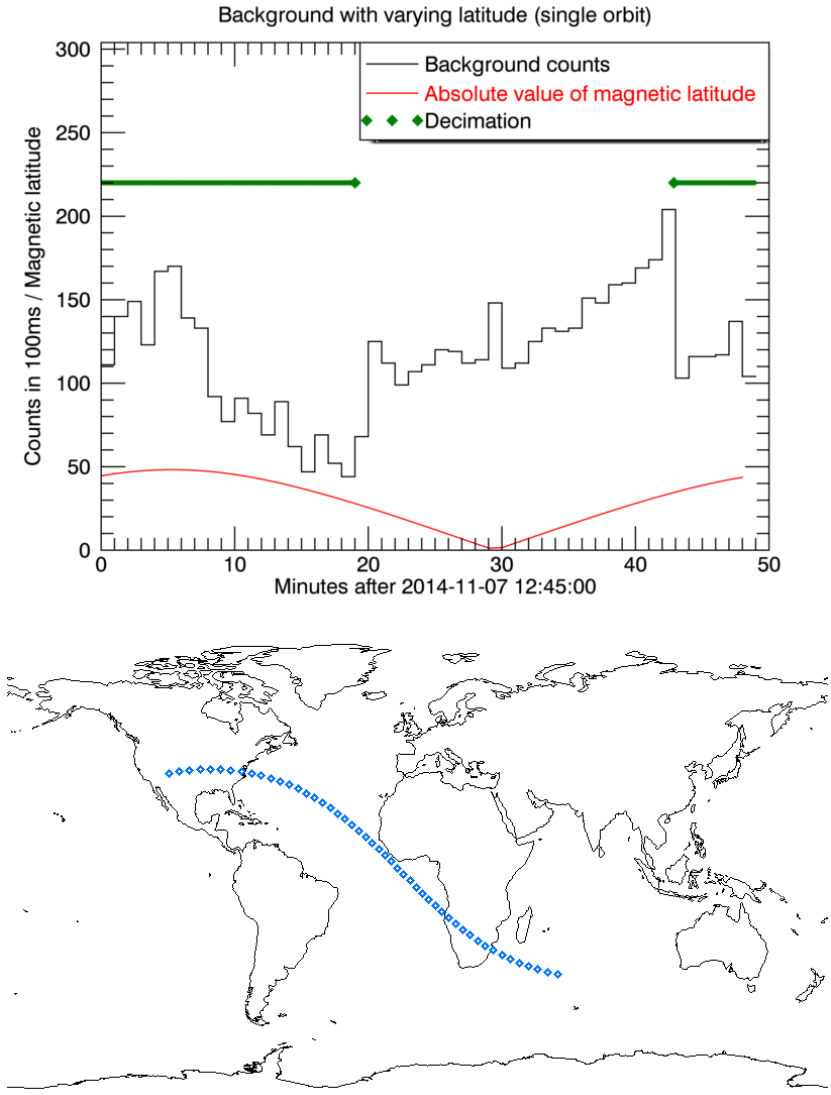

Fig. 6.10: Counts in 100 ms background for varying magnetic latitude in the course of one half orbit of RHESSI. The absolute value of the magnetic latitude is shown in red, and times with decimation in dark green. The geographic location of the orbit can be seen on the bottom.

Since the background levels at non-decimated times are significantly higher than the mean of the background distribution we see in Figure 6.2, we conclude that decimation must happen quite frequently, and correcting for this might be useful in future work. Since high latitudes have higher background rates, decimation is active more often in these regions. This explains the lower mean of the high northern latitudes in Figure 6.8.

Multiple orbits

To investigate the effect decimation has on the background distribution, we used the same method, but instead of doing a single half orbit, we used a span of 4000 minutes, starting at the same time of June 5th 2012 used in Figure 6.9. 4000 minutes correspond to about 42 of RHESSI's orbits, or 2.8 days. The first 500 minutes of this can be seen in Figure 6.11.

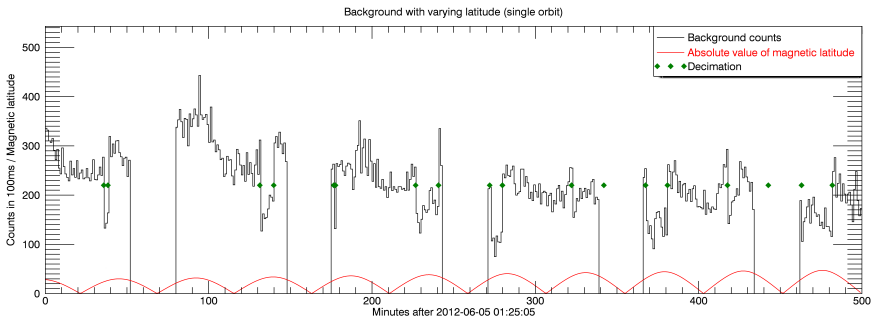

Fig. 6.11: Counts in 100 ms background in the course of 500 minutes. The absolute value of the magnetic latitude is shown in red, and the start and end times of decimation state are shown as dark green diamonds. The intervals with zero counts are the transits through the SAA where RHESSI's instruments are shut off.

We then removed every time interval from the SAA, as well as every interval where decimation was taking place. This left us with 1673 intervals of 100 ms. The distribution of the number of events for each of these intervals is given in Figure 6.12. As can be seen, the distribution without decimated events is much closer to a normal distribution than what we have previously seen. The mean of the non-decimated events is notably higher than that of

the first distribution presented in Figure 6.2. This also leads to the Poisson distribution being wider for these values.

The 4000 minute interval does not yield enough events to meaningfully split the distribution into different intervals of magnetic latitude. The interval was not increased due to the computational resources that would require.

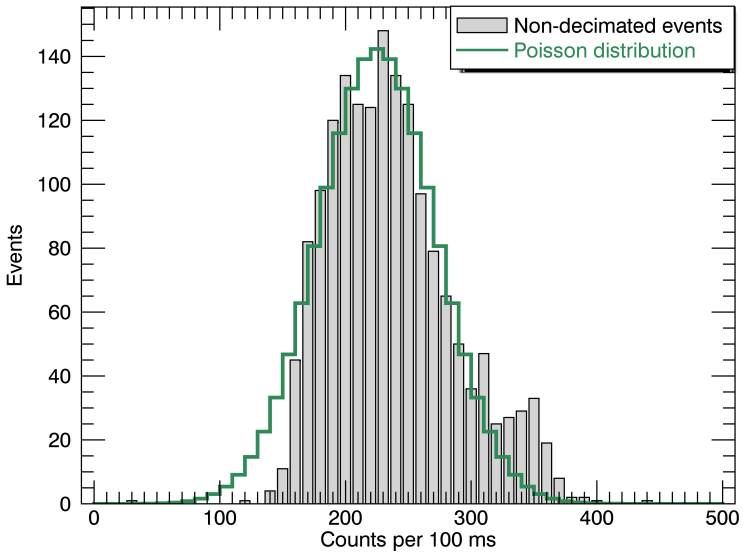

Fig. 6.12: Counts in 100ms background for non-decimated events (grey) with a Poisson distribution for the same number of events outlined in green.

6.3 Geographical distribution of TGFs

Lightning activity and the characteristics of thunderstorms differ over land and over ocean. Examples of this is differences in flash rates [*Christian et al.*, 2003], differences in the occurrences of Transient Luminous Events [*Chen et al.*, 2008], and difference in storm sizes [*Bang and Zipser*, 2015].

With this in mind, it is interesting to see whether TGFs follow an ocean/land pattern. We have defined a coastal zone of ±150 km from the coastline, which

dispels the ambiguity caused by coastal storm systems lying partially over the ocean, partially on land. We described the method for placing WWLLN registrations on the map and within the zones ocean, coast, and land in Section 5.4.

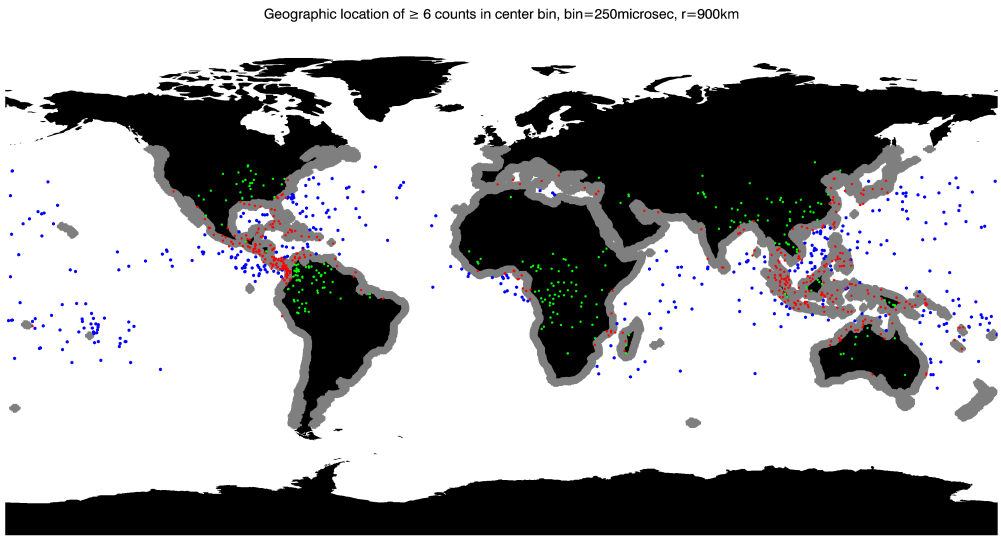

Fig. 6.13: The geographical distribution over ocean (blue), coast (red) and land (green) of the instances of lightning where RHESSI have six counts or more at the time of WWLLN registration. The coastal zone is defined as ±150 km from the coastline.

Here we use TGFs with a maximum radius from the subsatellite point of 900 km, a binsize of 250 μs and a minimum of six counts in the center bin, being the criteria we decided on in Section 6.1.1. TGFs from the Gjesteland catalog are removed. The geographical distribution can be seen in Figure 6.13. We note that as expected the TGFs seem to concentrate around areas of high lightning activity in the Caribbean and Indian oceans and Central Africa [*Christian et al.*, 2003].

The numerical and percentage distribution of the TGFs across the three geographical zones is given in Table 6.3. As can be seen, TGFs in the coastal zone are overrepresented compared to the amount of lightning in coastal zones in the years 2002–2015, (35.18%, see Table 6.4).

	TGFs	Percentage of total
Ocean	413	37.34%
Coast	480	43.40%
Land	213	19.26%
Total	1106	

Table 6.3: The distribution over ocean, coast and land of the instances of lightning where RHESSI have six counts or more at the time of WWLLN registration.

When comparing the TGFs to the WWLLN location it is worth noting how WWLLN's detection efficiency has changed geographically through the years. As was mentioned in Section 4.1, detection efficiency started out much higher in the Indian Ocean area, before expanding world wide. Because of the high amount of islands, disproportionally much of the area is considered coastal zone, as can be seen in Table 6.4 and in Figure 6.14. As the years progress and the detection efficiency improves, the detection of lightning across the three zones evens out.

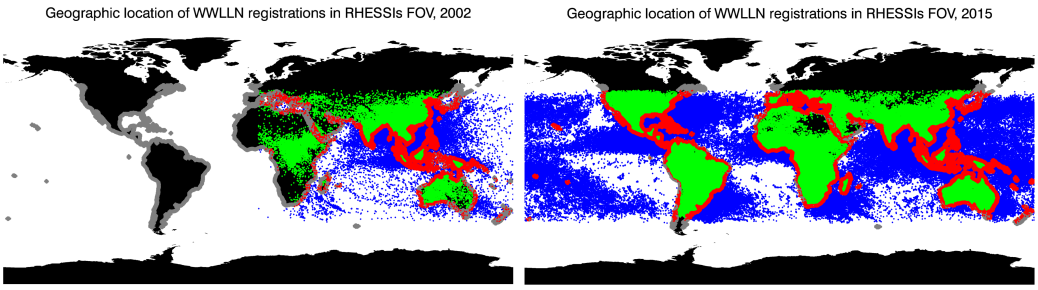

Fig. 6.14: The geographical of all WWLLN registrations within RHESSI's field of view in 2002 (left) and 2015 (right). Events over ocean are blue, over coast are red and over land are green.

Splitt et al. [2010] did a similar geographical distribution of RHESSI TGFs from 2002 to 2007, but without the WWLLN matches, giving a positional uncertainty the size of RHESSI's field-of-view. They used a coastal zone of 370 km, and found that TGFs were common near tropical coasts and islands.

Briggs et al. [2013] studied the distribution of Fermi TGFs in the Caribbean

Ocean, Central Africa and Oceania, and they also noted a trend towards coastal areas. They found the coastal dependence to be especially strong over Oceania, while Central Africa had more TGFs over land.

Hazelton [2009], using lightning registrations from the Lightning Imaging Sensor (LIS) aboard the satellite TRMM, found that RHESSI TGFs were "more likely to be produced over coastal regions than over land" compared to lightning. We find this to be consistent with our results. *Hazelton* [2009] did not find the higher occurrence of TGFs than lightning over ocean that we can see, but they also used a different classification system for the coast, operating with two radii of 300 km and 600 km.

		WWLLN Registrations	**Percentage of total**
2002	**Ocean**	29690	22.53%
	Coast	53347	45.87%
	Land	33275	28.60%
	Total	116312	
2015	**Ocean**	571457	31.23%
	Coast	606915	33.17%
	Land	651556	35.60%
	Total	1829928	
All years	**Ocean**	3964715	32.27%
	Coast	4322827	35.18%
	Land	3999821	32.55%
	Total	12287363	

Table 6.4: The distribution over ocean, coast and land of all WWLLN registrations within RHESSI's field of view in 2002 and 2015, as well as the distribution across all years 2002–2015.

Chapter 7

Summary

In this thesis we have applied the method of superposing data intervals from the satellite RHESSI at the time of lightning registration from the detector network WWLLN described by *Østgaard et al.* [2015] to the years 2002–2015. We have identified 1106 events which likely are weak signal TGFs not accounted for by the algorithms behind the TGF catalogs of *Grefenstette et al.* [2009] and *Gjesteland et al.* [2012].

We have provided a statistical analysis to optimize the values for binsize and maximum distance of lightning from the subsattelite point to use when searching for weak TGFs. We concluded that a binsize of 250 μs and a maximum distance of 900 km gave the strongest signal compared to background levels.

Because of the weak signal of the events we work with, they are difficult to distringuish from background radiation. We have identified several factors contributing to variation of the background levels RHESSI register, notably variation after annealings, variation with magnetic latitude, and the decimation process RHESSI uses to save memory.

We have also studied the geographical distribution of the TGFs we identified, focusing on their distribution across the zones ocean, coast and land. We found that a larger portion of TGFs occur in coastal areas than lightning in general, which is in agreement with literature.

Bibliography

Abarca, S. F., K. L. Corbosiero, and T. J. Galarneau (2010), An evaluation of the Worldwide Lightning Location Network (WWLLN) using the National Lightning Detection Network (NLDN) as ground truth, *Journal of Geophysical Research: Atmospheres*, *115*(18), 1–11, doi:10.1029/2009JD013411.

Bang, S. D., and E. J. Zipser (2015), Differences in size spectra of electrified storms over land and ocean, *Geophysical Research Letters*, *42*(16), 6844–6851, doi:10.1002/2015GL065264, 2015GL065264.

Boccippio, D. J., K. L. Cummins, H. J. Christian, and S. J. Goodman (2001), Combined satellite- and surface-based estimation of the intracloudcloud-to-ground lightning ratio over the continental united states, *Monthly Weather Review*, *129*(1), 108–122, doi:10.1175/1520-0493(2001)129⟨0108:CSASBE⟩2.0.CO;2.

Briggs, M. S., et al. (2013), Terrestrial gamma-ray flashes in the Fermi era: Improved observations and analysis methods, *Journal of Geophysical Research: Space Physics*, *118*(6), 3805–3830, doi:10.1002/jgra.50205.

Celestin, S., and V. P. Pasko (2011), Energy and fluxes of thermal runaway electrons produced by exponential growth of streamers during the stepping of lightning leaders and in transient luminous events, *Journal of Geophysical Research: Space Physics*, *116*(3), 1–14, doi:10.1029/2010JA016260.

Chen, A. B., et al. (2008), Global distributions and occurrence rates of transient luminous events, *Journal of Geophysical Research: Space Physics*, *113*(A8), n/a–n/a, doi:10.1029/2008JA013101, a08306.

Christian, H. J., et al. (2003), Global frequency and distribution of lightning as observed from space by the optical transient detector, *Journal of Geophysical Research: Atmospheres*, *108*(D1), ACL 4–1–ACL 4–15, doi: 10.1029/2002JD002347, 4005.

Cooray, V. (2003), *The Lightning Flash*, 574 pp., Institute of Electrical and Electronic Engineers, doi:10.1049/PBPO034E.

Dowden, R. L., J. B. Brundell, and C. J. Rodger (2002), VLF lightning location by time of group arrival (TOGA) at multiple sites, *Journal of Atmospheric and Solar-Terrestrial Physics*, *64*(7), 817–830, doi:10.1016/S1364-6826(02)00085-8.

Dwyer, J. R. (2003), A fundamental limit on electric fields in air, *Geophysical Research Letters*, *30*(20), 2055, doi:10.1029/2003GL017781.

Dwyer, J. R., and D. M. Smith (2005), A comparison between Monte Carlo simulations of runaway breakdown and terrestrial gamma-ray flash observations, *Geophysical Research Letters*, *32*(22), 1–4, doi:10.1029/2005GL023848.

Dwyer, J. R., and M. A. Uman (2014), The physics of lightning, *Physics Reports*, *534*, 147–241, doi:10.1016/j.physrep.2013.09.004.

Dwyer, J. R., D. M. Smith, and S. A. Cummer (2012), High-energy atmospheric physics: Terrestrial gamma-ray flashes and related phenomena, *Space Science Reviews*, *173*(1-4), 133–196, doi:10.1007/s11214-012-9894-0.

Fishman, G., et al. (1989), The burst and transient source experiment (batse)-scientific objectives and capabilities, in *GRO Science Workshop (Greenbelt: GSFC)*, vol. 3.

Fishman, G. J., et al. (1994), Discovery of intense gamma-ray flashes of atmospheric origin., *Science (New York, N.Y.)*, *264*(5163), 1313–1316, doi:10.1126/science.264.5163.1313.

Gjesteland, T., N. Østgaard, a. B. Collier, B. E. Carlson, C. Eyles, and D. M. Smith (2012), A new method reveals more TGFs in the RHESSI data, *Geophysical Research Letters*, *39*(5), n/a–n/a, doi:10.1029/2012GL050899.

Gjesteland, T., N. Østgaard, R. Nisi, A. Collier, and G. Lu (2014), Twelve Years of RHESSI TGFs The Second RHESSI TGF Catalog, *EGU General Assembly*, *16*, 14,125, doi:10.1029/2011JA016612.

Grefenstette, B. W., D. M. Smith, B. J. Hazelton, and L. I. Lopez (2009), First RHESSI terrestrial gamma ray flash catalog, *Journal of Geophysical Research: Space Physics*, *114*(2), A02,314, doi:10.1029/2008JA013721.

Gurevich, A., G. Milikh, and R. Roussel-Dupre (1992), Runaway electron mechanism of air breakdown and preconditioning during a thunderstorm, *Physics Letters A*, *165*(5), 463 – 468, doi:http://dx.doi.org/10.1016/0375-9601(92)90348-P.

Hazelton, B. (2009), Statistical studies and modeling of RHESSI Terrestrial Gamma-ray Flashes, [Doctoral dissertation, UMI Number: 3368456].

Lay, E. H., A. R. Jacobson, R. H. Holzworth, C. J. Rodger, and R. L. Dowden (2007), Local time variation in land/ocean lightning flash density as measured by the world wide lightning location network, *Journal of Geophysical Research: Atmospheres*, *112*(D13), n/a–n/a, doi:10.1029/2006JD007944, d13111.

Lin, R., et al. (2002), The reuven ramaty high-energy solar spectroscopic imager (rhessi), *Solar Physics*, *210*(1), 3–32, doi:10.1023/A:1022428818870.

Mallick, S., et al. (2014), Evaluation of the WWLLN Performance Characteristics Using Rocket-Triggered Lightning Data, *International Conference on Grounding and Earthing and 6th International Conference on Lightning Physics and Effects*.

Marisaldi, M., et al. (2010), Detection of terrestrial gamma ray flashes up to 40 MeV by the AGILE satellite, *Journal of Geophysical Research*, *115*, A00E13, doi:10.1029/2009JA014502.

Marisaldi, M., et al. (2015), Enhanced detection of terrestrial gamma-ray flashes by agile, *Geophysical Research Letters*, *42*(21), 9481–9487, doi:10.1002/2015GL066100, 2015GL066100.

Marshall, T. C., M. P. McCarthy, and W. D. Rust (1995), Electric field magnitudes and lightning initiation in thunderstorms, *Journal of Geophysical Research*, *100*(D4), 7097–7103, doi:10.1029/95JD00020.

McCarthy, M. P., and G. K. Parks (1992), On the modulation of x ray fluxes in thunderstorms, *Journal of Geophysical Research: Atmospheres*, *97*(D5), 5857–5864, doi:10.1029/91JD03160.

McTague, L. E., S. A. Cummer, M. S. Briggs, V. Connaughton, M. Stanbro, and G. Fitzpatrick (2015), A lightning-based search for nearby observationally dim terrestrial gamma ray flashes, *Journal of Geophysical Research: Atmospheres*, *120*(23), 12,003–12,017, doi:10.1002/2015JD023475, 2015JD023475.

Mezentsev, A., N. Østgaard, T. Gjesteland, K. Albrechtsen, N. Lehtinen, M. Marisaldi, D. Smith, and S. Cummer (2016), Radio emissions from double rhessi tgfs, *Journal of Geophysical Research: Atmospheres*, *121*(13), 8006–8022, doi:10.1002/2016JD025111, 2016JD025111.

Moss, G. D., V. P. Pasko, N. Liu, and G. Veronis (2006), Monte Carlo model for analysis of thermal runaway electrons in streamer tips in transient luminous events and streamer zones of lightning leaders, *Journal of Geophysical Research: Space Physics*, *111*(2), 1–37, doi:10.1029/2005JA011350.

NASA (a), About the Compton Gamma Ray Observatory, url = https://heasarc.gsfc.nasa.gov/docs/cgro/cgro/, [Online; accessed 25-May-2017].

NASA (b), BATSE Triggers, url = https://gammaray.nsstc.nasa.gov/batse/misc/triggers.html, [Online; accessed 25-May-2017].

NASA (c), RHESSI, url = https://hesperia.gsfc.nasa.gov/rhessi3/, [Online; accessed 25-May-2017].

NASA (d), RHESSI STATUS, url = https://hesperia.gsfc.nasa.gov/rhessi3/news-and-resources/status/index.html, [Online; accessed 25-May-2017].

Neubert, T., I. Kuvvetli, C. Budtz-Jørgensen, N. Østgaard, V. Reglero, and N. Arnold (2006), The atmosphere-space interactions monitor (asim) for the international space station, *ILWS Workshop*.

Østgaard, N., T. Gjesteland, J. Stadsnes, P. H. Connell, and B. Carlson (2008), Production altitude and time delays of the terrestrial gamma flashes: Revisiting the burst and transient source experiment spectra,

Journal of Geophysical Research: Space Physics, *113*(A2), n/a–n/a, doi: 10.1029/2007JA012618, a02307.

Østgaard, N., T. Gjesteland, R. S. Hansen, a. B. Collier, and B. Carlson (2012), The true fluence distribution of terrestrial gamma flashes at satellite altitude, *Journal of Geophysical Research*, *117*(A3), A03,327, doi: 10.1029/2011JA017365.

Østgaard, N., T. Gjesteland, B. E. Carlson, a. B. Collier, S. a. Cummer, G. Lu, and H. J. Christian (2013), Simultaneous observations of optical lightning and terrestrial gamma ray flash from space, *Geophysical Research Letters*, *40*(10), 2423–2426, doi:10.1002/grl.50466.

Østgaard, N., K. H. Albrecthsen, T. Gjesteland, and A. Collier (2015), A new population of terrestrial gamma-ray flashes in the rhessi data, *Geophysical Research Letters*, *42*(24), 10,937–10,942, doi:10.1002/2015GL067064, 2015GL067064.

Pinçon, J. L., E. Blanc, P. L. Blelly, M. Parrot, J. L. Rauch, J. A. Savaud, and E. Séran (2011), Taranis x2014; scientific payload and mission strategy, in *2011 XXXth URSI General Assembly and Scientific Symposium*, pp. 1–4, doi:10.1109/URSIGASS.2011.6050938.

Quick, M., R. J. Blakeslee, H. J. Christian, Jr., M. F. Stewart, S. Podgorny, and D. Corredor (2015), Airborne GLM Simulator (FEGS), *AGU Fall Meeting Abstracts*.

Rakov, V., and M. Uman (2003), *Lightning: Physics and effects*.

Smith, D., L. Lopez, R. Lin, and C. Barrington-Leigh (2005), Terrestrial gamma-ray flashes observed up to 20 MeV, *Science*, *307*(February), 1085–1089.

Smith, D. M., et al. (2002), The RHESSI spectrometer, *Solar Physics*, *210*(1-2), 33–60, doi:10.1023/A:1022400716414.

Smith, D. M., B. J. Hazelton, B. W. Grefenstette, J. R. Dwyer, R. H. Holzworth, and E. H. Lay (2010), Terrestrial gamma ray flashes correlated to storm phase and tropopause height, *Journal of Geophysical Research: Space Physics*, *115*(A8), n/a–n/a, doi:10.1029/2009JA014853, a00E49.

Smith, D. M., et al. (2011), A terrestrial gamma ray flash observed from an aircraft, *Journal of Geophysical Research*, *116*(D20), D20,124, doi:10.1029/2011JD016252.

Smith, D. M., P. Buzbee, N. A. Kelley, A. Infanger, R. H. Holzworth, and J. R. Dwyer (2016), The rarity of terrestrial gamma-ray flashes: 2. rhessi stacking analysis, *Journal of Geophysical Research: Atmospheres*, *121*(19), 11,382–11,404, doi:10.1002/2016JD025395, 2016JD025395.

Splitt, M. E., S. M. Lazarus, D. Barnes, J. R. Dwyer, H. K. Rassoul, D. M. Smith, B. Hazelton, and B. Grefenstette (2010), Thunderstorm characteristics associated with rhessi identified terrestrial gamma ray flashes, *Journal of Geophysical Research: Space Physics*, *115*(A6), n/a–n/a, doi:10.1029/2009JA014622, a00E38.

Stanley, M. a., X. M. Shao, D. M. Smith, L. I. Lopez, M. B. Pongratz, J. D. Harlin, M. Stock, and A. Regan (2006), A link between terrestrial gamma-ray flashes and intracloud lightning discharges, *Geophysical Research Letters*, *33*(6), 1–5, doi:10.1029/2005GL025537.

Tavani, M., et al. (2011), Terrestrial gamma-ray flashes as powerful particle accelerators, *Physical Review Letters*, *106*(1), 1–5, doi:10.1103/PhysRevLett.106.018501.

Wilson, C. T. R. (1924), The electric field of a thundercloud and some of its effects, *Proceedings of the Physical Society of London*, *37*(1), 32D–37D, doi:10.1088/1478-7814/37/1/314.